NeuroImage 211 (2020) 116606

Contents lists available at ScienceDirect

NeuroImage

journal homepage: www.elsevier.com/locate/neuroimage

Quasi-diffusion magnetic resonance imaging (QDI): A fast, high b-value diffusion imaging technique

Thomas R. Barrick [a,*], Catherine A. Spilling [a], Carson Ingo [b,c], Jeremy Madigan [d], Jeremy D. Isaacs [a,e], Philip Rich [d], Timothy L. Jones [f], Richard L. Magin [g], Matt G. Hall [h,i], Franklyn A. Howe [a]

[a] Neurosciences Research Centre, Molecular and Clinical Sciences Research Institute, St George's, University of London, London, UK
[b] Department of Neurology, Northwestern University, Chicago, USA
[c] Department of Physical Therapy and Human Movement Sciences, Northwestern University, Chicago, USA
[d] Department of Neuroradiology, St George's University Hospitals NHS Foundation Trust, London, UK
[e] Department of Neurology, St George's University Hospitals NHS Foundation Trust, London, UK
[f] Department of Neurosurgery, St George's University Hospitals NHS Foundation Trust, London, UK
[g] Department of Bioengineering, University of Illinois at Chicago, USA
[h] Great Ormond Street Institute of Child Health, University College London, London, UK
[i] National Physical Laboratory, Teddington, UK

ARTICLE INFO

Keywords:
Magnetic resonance imaging
Brain
Continuous time random walk
Non-Gaussian diffusion
Diffusional kurtosis imaging
High b-value

ABSTRACT

To enable application of non-Gaussian diffusion magnetic resonance imaging (dMRI) techniques in large-scale clinical trials and facilitate translation to clinical practice there is a requirement for fast, high contrast, techniques that are sensitive to changes in tissue structure which provide diagnostic signatures at the early stages of disease. Here we describe a new way to compress the acquisition of multi-shell b-value diffusion data, Quasi-Diffusion MRI (QDI), which provides a probe of subvoxel tissue complexity using short acquisition times (1–4 min). We also describe a coherent framework for multi-directional diffusion gradient acquisition and data processing that allows computation of rotationally invariant quasi-diffusion tensor imaging (QDTI) maps.

QDI is a quantitative technique that is based on a special case of the Continuous Time Random Walk model of diffusion dynamics and assumes the presence of non-Gaussian diffusion properties within tissue microstructure. QDI parameterises the diffusion signal attenuation according to the rate of decay (i.e. diffusion coefficient, D in $mm^2\ s^{-1}$) and the shape of the power law tail (i.e. the fractional exponent, α). QDI provides analogous tissue contrast to Diffusional Kurtosis Imaging (DKI) by calculation of normalised entropy of the parameterised diffusion signal decay curve, H_n, but does so without the limitations of a maximum b-value.

We show that QDI generates images with superior tissue contrast to conventional diffusion imaging within clinically acceptable acquisition times of between 84 and 228 s. We show that QDI provides clinically meaningful images in cerebral small vessel disease and brain tumour case studies. Our initial findings suggest that QDI may be added to routine conventional dMRI acquisitions allowing simple application in clinical trials and translation to the clinical arena.

1. Introduction

Over the last decade there have been extensive advances in acquisition and analysis of diffusion magnetic resonance imaging (dMRI) data but these have not been routinely translated into clinical practice. One reason for this is the frequently lengthy acquisition times required to provide adequate image quality. This can be prohibitive, for example, in acute stroke where there is a need for rapid data acquisition as patients are not always able to remain motionless throughout lengthy MRI protocols. Consequently, current clinical use of dMRI is limited to conventional Diffusion-Weighted Imaging (DWI) (i.e. clinical trace DWI) and the occasional use of Diffusion Tensor Imaging (DTI). To enable application

* Corresponding author. Neurosciences Research Centre, Molecular and Clinical Sciences Research Institute, St George's, University of London, Cranmer Terrace, London, SW17 0RE, UK.
E-mail address: tbarrick@sgul.ac.uk (T.R. Barrick).

https://doi.org/10.1016/j.neuroimage.2020.116606
Received 18 September 2019; Received in revised form 22 December 2019; Accepted 2 February 2020
Available online 4 February 2020

of new dMRI techniques in large-scale clinical trials and facilitate translation to clinical practice there is the requirement to provide high signal to noise and high contrast to noise using short acquisition times (i.e. between 1 and 4 min). Here we introduce a novel dMRI technique, Quasi-Diffusion MRI (QDI), which utilises a rapid scan acquisition that can be acquired on clinical MR systems and provides high tissue contrast images. The QDI technique provides a coherent framework for data acquisition and processing to give all conventional dMRI contrasts plus images analogous to Diffusional Kurtosis Imaging (DKI) (Jensen et al., 2005; Jensen and Helpern, 2010).

The simplest and most widespread assumption used in dMRI analysis is that spin displacements are Gaussian (Jones et al., 2013; Johansen-Berg and Behrens, 2009) leading to prediction of mono-exponential diffusion signal attenuation with b-value (Callaghan, 2011). DWI and DTI use this assumption and can be routinely acquired in the clinic in 1–4 min. Although mono-exponential signal decay is observed in diffusion-weighted measurements of fluids, this is not the case for diffusion in more structurally complex media such as tissue, where the signal decays more slowly than described by a single exponential function and a Gaussian process alone (Clark and Le Bihan, 2000).

The observation of non-mono-exponential decay has led to the concept that diffusion is influenced by microstructure which impedes the motion of spins. Structures with a size similar to the typical diffusion length-scale will impede spins' motion in a non-trivial way (e.g. Grebenkov, 2009, 2008) and cause departures from a Gaussian displacement distribution. This has led to the diffusion signal being used as a probe of microstructural properties of the tissue environment by techniques that model underlying tissue geometry (e.g. biexponential (Clark and Le Bihan, 2000), CHARMED (Assaf and Basser, 2005), AxCaliber (Assaf et al., 2008), ActiveAx (Alexander, 2008; Alexander et al., 2010), NODDI (Zhang et al., 2012), VERDICT (Panagiotaki et al., 2015, 2014)). These techniques potentially provide useful clinical information but require lengthy dMRI acquisition times due to the requirement for numerous diffusion gradient directions and b-value shells. In addition, techniques such as NODDI exhibit acquisition and parameter-based bias (Jelescu et al., 2015; Jelescu and Budde, 2017) and are not readily applicable to organs outside the central nervous system without adaption of geometrical assumptions and algorithmic recalibration (Bonet-Carne et al., 2019). Multidimensional dMRI (Topgaard, 2017) is a technique derived from multidimensional solid-state MRI that uses q-vector trajectory encoding MRI acquisition sequences to provide a representation of diffusion in isotropic and directional tissue dimensions. This technique is not yet clinically available and requires lengthy acquisition times and requires gradient pulse shapes to be optimised using bespoke software and uploaded to the scanner prior to any application.

Another recent approach is to make an assumption regarding the overall distribution of barriers in the environment and estimate a time-dependent diffusivity (Novikov and Kiselev, 2010; Novikov et al., 2011, 2014, 2019). In this case a model is derived that involves a diffusivity with a power-law time dependence. Model parameters are estimated from diffusion-weighted measurements at several diffusion times, and the power-law exponent is related to the presence or absence of disorder in the diffusion environment. The strength of this approach and that of Topgaard (2017) is that no geometric assumptions regarding the tissue microstructure are necessary. The technique has been applied in humans to estimate muscle fibre size (Sigmund et al., 2014), prostate microstructure (Lemberskiy et al., 2018) and properties of the human brain (Veraart et al., 2019). One disadvantage, however, is the requirement for dMRI acquisition at multiple diffusion times resulting in lengthy acquisition times.

An alternative to these techniques is DKI, which provides a representation (rather than a biophysical model, Novikov et al., 2018a) of non-Gaussian diffusion (Jensen et al., 2005; Jensen and Helpern, 2010). DKI provides greater sensitivity to subtle microstructural damage than DTI in early detection of pathological change (Gong et al., 2017; Praet et al., 2018) and histological grade of brain tumours (Falk Delgado et al., 2018). This technique adds a fourth order moment to the second order mono-exponential diffusion decay curve and computes an additional term, κ, representing departures from Gaussian diffusion due to interactions with the microstructural environment. However, the technique has several limitations: (i) DKI provides unreliable information for $b > 3000$ s mm^{-2} (Jensen and Helpern, 2010) and (ii) DKI has frequent fitting errors that lead to computation of negative kurtosis within an image voxel (Jensen and Helpern, 2010; Tabesh et al., 2011). The first issue represents a limitation for clinical studies as dMRI of ultra-high b-values (i.e. $b > 3000$ s mm^{-2}) has potential in characterising neurodegenerative diseases such as Parkinson's disease (Xueying et al., 2015) and Alzheimer's disease (Yingnan et al., 2018), and characterising brain tumour subtypes (Tan et al., 2018). Secondly, although DKI acquisitions have a theoretical minimum acquisition of 15 diffusion gradient directions in 3 b-values (i.e. $b = 0$ s mm^{-2} and two non-zero b-value shells), a routine acquisition typically involves 30 or more directions in more than two non-zero b-value shells. These limitations mean that DKI cannot use the higher diffusion sensitisation capabilities of modern clinical MRI systems and does not provide a time efficient scan acquisition.

Our QDI technique has different assumptions with respect to the underlying diffusion process. We apply a special case of a general model of diffusion dynamics based on anomalous transport theory (Gorenflo et al., 2002; Metzler and Klafter, 2000; Zaslavsky, 2005; Klages et al., 2008) in which the continuous-time random walk (CTRW) model describes the dynamics of the diffusing spins based on fractional calculus (Klages et al., 2008). The CTRW model makes no explicit microstructural assumptions but instead assumes an effective diffusion process. This provides a generalised diffusion equation and propagator in which the mean-squared displacement of spins depends on some (non-integer) powers of time and space. Diffusion dynamics are described by two processes that are represented by fractional exponents: α representing the probability density function (pdf) of waiting times and β representing the pdf of step lengths in their random walks. The CTRW model has been applied to dMRI data but typically involves acquisition of more than two non-zero b-value shells across multiple diffusion gradient directions (ex-vivo: Ingo et al., 2014b; Gatto et al., 2019; in-vivo: Karaman et al., 2016; Tang and Zhou, 2019) and hence requires lengthy acquisition times. Furthermore, dMRI acquisition parameterised by diffusion gradient strength and diffusion time may be necessary for accurate quantification of model parameters (Ingo et al., 2014b) further increasing acquisition time.

We impose a special case of the CTRW model by assuming there is a scaling relationship between time and space for diffusion in tissue microstructure. We do this both for practical and theoretical reasons. The special case is achieved by identifying a relationship between α and β, specifically $\beta = 2\alpha$, which describes a quasi-diffusion random-walk model of the diffusion dynamics for coupled random walks (Jurlewicz et al., 2012; Luchko et al., 2016; Meerschaert and Scheffler, 2019). This relationship simplifies the CTRW model and establishes a mean-squared displacement of spins that is linearly proportional to time but for which, in general, the diffusion signal decay is slower than for mono-exponential Gaussian diffusion. This quasi-diffusion model represents non-Gaussian diffusion dynamics in a heterogeneous medium and parameterises signal attenuation according to the quantitative measures of rate of decay (i.e. the diffusion coefficient, D in mm^2 s^{-1}) and the shape of the power law tail (i.e. the fractional exponent, α). We can consider quasi-diffusion either as a model based on emergent diffusion dynamics, or as a representation of dMRI data (Novikov et al., 2018a) which is more compact than DKI and provides a better parameterisation of diffusion signal attenuation at high b-values. To enable QDI to provide tissue contrast similar to κ we compute the normalised entropy of the parameterised diffusion signal decay curve, H_n (Ingo et al., 2014b, 2014a). An advantage of the QDI technique is that it estimates D and α separately in *each* diffusion gradient direction and requires a minimum acquisition of a $b = 0$ s mm^{-2} image followed by two non-zero b-value shells, allowing rapid dMRI acquisition in clinically acceptable time. QDI may be applied to any

b-value range and Quasi-Diffusion Weighted Imaging (QDWI) and Quasi-Diffusion Tensor Imaging (QDTI) maps analogous to conventional diffusion modalities are computed.

Here we provide the theoretical background to QDI and show the proof of concept of the technique. We show QDTI maps for healthy volunteers and provide an estimate of variance in brain tissue. We then show that QDTI provides maps analogous to DKI and that QDTI is capable of estimating D and α within image voxels where DKI fails. We also consider the performance of QDI for minimal dMRI acquisition schemes (using SENSE to speed up the acquisition, but without multi-band imaging) in 15, 6 and 3 diffusion gradient directions (i.e. in 228s, 120s and 84s, respectively) indicating the potential clinical feasibility of the technique. Finally, we present clinical case studies for six diffusion gradient direction QDTI in cerebral small vessel disease (SVD) and brain tumour patients.

2. Methods

2.1. Theory

2.1.1. Continuous time random walk model of diffusion dynamics

In this study we use a general model of the underlying diffusion process known as the continuous time random walk (CTRW). The crucial difference between the CTRW and conventional random walks models is that the mean-squared displacement of diffusing particles depends on some (non-integer) power of time (Metzler and Klafter, 2000; Klages et al., 2008). This model gives a generalised form,

$$\langle x\rangle^{2\sim}t^{2\alpha/\beta} \qquad \text{[Eq. 1]}$$

where diffusion dynamics are described by two exponents: α which defines the pdf of waiting times between steps in random walks and β which defines the pdf of step lengths. Diffusing particles execute a step, and then remain stationary for a short time before taking another. The exponents are assumed to be independent, and both processes are described by an inverse power dependency for step length, $x^{\beta-2}$, and waiting time $t^{\alpha-1}$. This means that large step lengths and waiting times are much less likely than shorter ones but are nevertheless more likely than for a Gaussian distribution. The model reduces to Gaussian distributions when $\alpha = 1$ and $\beta = 2$.

2.1.2. Application of the continuous time random walk diffusion model to dMRI

Following an analogous strategy to Gaussian diffusion the 1D motion of a diffusing particle, $P(x,t)$, is represented by a fractional partial differential equation (see Ingo et al., 2014b for details). For application to dMRI the Fourier Transform of this solution is derived in q-space where $q = \frac{1}{2\pi}\gamma g\delta$ (in mm^{-1}), γ is the gyromagnetic ratio of hydrogen, g is the diffusion gradient strength (in mTm^{-1}), and the effective diffusion time is denoted as $\overline{\Delta} = \Delta - \frac{\delta}{3}$ (in s) for a given diffusion gradient pulse duration, δ, and separation, Δ. This provides an equation for the diffusion signal decay, $p(q,\overline{\Delta})$ as follows,

$$p(q,\overline{\Delta}) = E_\alpha(-D_{\alpha,\beta}|q|^\beta\overline{\Delta}^\alpha) \qquad \text{[Eq. 2]}$$

where E_α is the single-parameter Mittag-Leffler function (MLF) (Haubold et al., 2011). The MLF is defined as a power series for $z \in \mathbb{C}$ such that,

$$E_\alpha(z) = \sum_{k=0}^{\infty}\frac{z^k}{\Gamma(\alpha k+1)} \qquad \text{[Eq. 3]}$$

where Γ(y) is the Gamma function, a generalization of the factorial function for all $y \in R$. At low z this equation describes a stretched exponential and at high z a power law decay (Carpinteri and Mainardi, 1997). In Eq. (2) the orders of the fractional operators α and β are fractional exponents that stretch and contract the power law tails of the waiting time and step length pdfs and allow inference of asymptotic microscopic diffusion dynamics from macroscopic experimental data (Mainardi et al., 2001; Klages et al., 2008; Gorenflo et al., 2014; Evangelista et al., 2018; Magin et al., 2019).

The fractional time and space exponents are decoupled and provide potentially uncorrelated α and β exponents that have meaning with respect to the type of diffusion that is present within a voxel (i.e. Gaussian, sub-diffusive (i.e. slower than Gaussian) or super-diffusive (i.e. faster than Gaussian), Fig. 1). Such a model ideally requires dMRI acquisition across multiple q and $\overline{\Delta}$ values (Ingo et al., 2014b) and is either not clinically feasible due to long acquisition times, or is affected by the limited range of diffusion times available on clinical MR systems (Magin et al., 2013). Furthermore, the diffusion coefficients, $D_{\alpha,\beta}$, computed from Eq. (2) are in units of $mm^\beta s^{-\alpha}$ and require complex methods to recover units of mm^2s^{-1} (e.g. Ingo et al., 2014b; Karaman et al., 2016; Magin et al., 2008). A pragmatic, clinically feasible solution to ensuring acquisition times are short is to keep $\overline{\Delta}$ constant and alter q, however, such a restriction still requires extensive data acquisition across multiple b-value shells (Gatto et al., 2019; Ingo et al., 2014b; Karaman et al., 2016; Tang and Zhou, 2019).

2.1.3. Quasi-diffusion MRI

We propose a simplification of the CTRW model by a coupling of the α and β exponents. Mean-squared displacement of diffusing particles in the CTRW model is given by $\langle x\rangle^2 \sim t^{\frac{2\alpha}{\beta}}$ and Gaussian diffusion by $\alpha = 1$ and $\beta = 2$, such that $\langle x\rangle^2 \sim t$. If the same heuristic Gaussian scaling relation of position with time continues to hold for non-Gaussian diffusion then $\langle x\rangle^2 \sim t$ and $2\alpha/\beta = 1$. In this case the model represents non-Gaussian diffusion which is not super-diffusive or sub-diffusive (see Fig. 1); instead we have a quasi-diffusion process. For dMRI the quasi-diffusion equation is derived by substitution of $\beta = 2\alpha$ in Eq. (2) as follows,

$$p(q,\overline{\Delta}) = \sum_{k=0}^{\infty}\frac{\left(-D_{\alpha,2\alpha}q^{2\alpha}\overline{\Delta}^\alpha\right)^k}{\Gamma(\alpha k+1)} = \sum_{k=0}^{\infty}\frac{(-1)^k(D_{1,2}b)^{\alpha k}}{\Gamma(\alpha k+1)}, \qquad \text{[Eq. 4]}$$

where signal attenuation is parameterised by $b = q^2\overline{\Delta}$ and the diffusion coefficient, $D_{1,2}$, is in conventional units of mm^2s^{-1}. The two variants of Eq. (4) allow fitting with respect to q- or b-value. The fractional α exponent represents a range of properties from Gaussian diffusion ($\alpha = 1$) through non-Gaussian (quasi) diffusion ($0 < \alpha < 1$). Specifically, QDI parameterises the signal decay by b-value according to the rate of decay, $D_{1,2}$, and the shape of the power law tail, α. Both $D_{1,2}$ and α are quantitative measures. It is important to note that α is analogous to the DKI κ measure as it represents non-Gaussian diffusion dynamics.

2.1.4. Normalised entropy

QDI does not explicitly allow derivation of diffusional kurtosis (see Ingo et al., 2015, 2014a), however, we can use the estimates of $D_{1,2}$ and α from Eq. (4) to predict diffusion signal attenuation at high b-values and so create synthetic images with contrast similar to κ. To achieve this we compute the information content in the fitted signal decay curve (i.e. a composite measure of the rate of decay and shape of the curve) as the normalised Shannon entropy $H_n(p(q,\overline{\Delta}))$ (Ingo et al., 2014b, 2014a),

$$H_n(p(q,\overline{\Delta})) = \frac{1}{log(N)}\int_{i=1}^{N}p(q_i,\overline{\Delta})ln(p(q_i,\overline{\Delta})), \qquad \text{[Eq. 5]}$$

where $0 \le H_n(p(q,\overline{\Delta})) \le 1$ and N is the total number of samples taken along the curve. The normalised entropy measure is not fully quantitative as it is affected by altering the number of samples along the curve or the range of q- or b-values it is computed across. Greater H_n values correspond to larger deviation of the signal decay curve from Gaussian

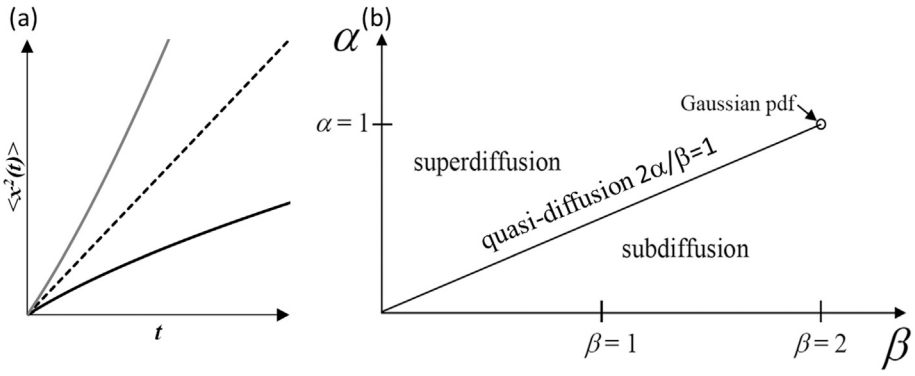

Fig. 1. Stochastic properties of diffusion processes that may be determined using the general CTRW model. Graph (a) shows mean-squared displacement with respect to diffusion time for sub-diffusion (black line), super-diffusion (grey line) and regular Gaussian diffusion (dotted line). Graph (b) shows the diffusion phase diagram and indicates the type of diffusion processes as identified by the time, α, and space, β, fractional exponents (adapted from Metzler and Klafter, 2000). Regular Gaussian diffusion occurs when $\alpha = 1$ and $\beta = 2$, with super diffusion when $2\alpha/\beta > 1$ and sub diffusion when $2\alpha/\beta < 1$. Quasi-diffusion occurs when $2\alpha/\beta = 1$ (i.e. $2\alpha = \beta$).

diffusion. Intuitively, H_n, represents the complex heterogeneity of the diffusion environment.

2.1.5. Diffusion MRI acquisition strategies for QDI

The minimum number of MR images needed to estimate $D_{1,2}$ and α from Eq. (4) along a single diffusion gradient direction corresponds to dMRI acquisition at 3 b-values (e.g. b = 0 s mm^{-2} and 2 non-zero b-values). For QDWI there is a minimum requirement for 7 diffusion measurements (e.g. b = 0 s mm^{-2}, and 2 non-zero b-values in 3 orthogonal diffusion gradient directions). Similarly, a QDTI acquisition, which allows computation of $D_{1,2}$ and α tensor maps requires at least 13 diffusion measurements (e.g. b = 0 s mm^{-2}, and 2 non-zero b-values in 6 non-collinear diffusion gradient directions). Such a minimum QDTI acquisition requires considerably fewer dMRI acquisitions than DKI which requires a minimum of 31 measurements (e.g. b = 0 s mm^{-2}, and 2 non-zero b-values in 15 non-collinear diffusion gradient directions, Jensen and Helpern (2010)). QDTI can be acquired in 42% of the minimum DKI acquisition time allowing QDTI to be added to routine clinical protocols without significantly increasing the overall scanning time.

2.1.6. Quasi-diffusion tensor imaging

QDI includes dMRI acquisition along radial lines in q-space from which 1D estimates of $D_{1,2}$, α and H_n are computed. These estimates can be considered as spherical samples from which 3 × 3 tensors may be computed (Hall and Barrick, 2012). $D_{1,2}$, α and H_n tensors are computed separately and provide 3 positive real eigenvalues, λ_1, λ_2 and λ_3, where $\lambda_1 > \lambda_2 > \lambda_3$, at each voxel with 3 corresponding eigenvectors, $\mathbf{v_1}$, $\mathbf{v_2}$ and $\mathbf{v_3}$. Familiar metrics are computed from the $D_{1,2}$ tensor as mean $D_{1,2} = (\lambda_1 + \lambda_2 + \lambda_3)/3$, axial $D_{1,2} = \lambda_1$, radial $D_{1,2} = (\lambda_2 + \lambda_3)/2$) and $D_{1,2}$ anisotropy (i.e. fractional anisotropy, Pierpaoli and Basser, 1996). Similar equations are used to calculate α metrics from the exponent tensor. For the normalised entropy tensor, mean H_n and H_n anisotropy are computed as above, but axial $H_n = \lambda_3$ is assumed to be aligned along the direction of least entropy, with radial $H_n = (\lambda_1 + \lambda_2)/2$). All QDTI measures are rotationally invariant.

2.2. Participants

Healthy subjects: Eight healthy participants were recruited (age 29 ± 8 years, 3 male, 5 female). Ethics approval was obtained for the study (East London 3 Research Ethics Committee (REC): 10/H0701/36) and written informed consent was obtained from each participant prior to MR scanning.

Cerebral small vessel disease patients: Two patients were recruited as part of the "Magnetic resonance spectroscopy to validate brain glutamate as a therapeutic target in delirium and dementia" study at St George' (SGUL) for which ethical approval was obtained (REC: 18/WA/0063). Written informed consent was obtained from each participant prior to MR scanning. Both participants had incidental findings of SVD on scanning. Case 1 (age 71 years) had extensive leukoariaosis. Case 2 (age 75 years) had an incidental acute ischaemic infarct.

Brain tumour patients: Three brain tumour patients were recruited as part of the "Tissue-type magnetic resonance imaging of brain tumours" study at SGUL for which ethical approval was obtained (South Central Hampshire REC: 17/SC/0460). Written informed consent was obtained from each participant prior to MR scanning. Case 1 (age 72 years) had two WHO Grade I meningiomas (one angiomatous, the other psammomatous), case 2 (age 40 years) had a WHO Grade II astrocytoma, and case 3 (age 58 years) had a WHO Grade IV glioblastoma.

2.3. Magnetic resonance image acquisition

MR images were acquired on a 3T Philips Achieva Dual TX MR scanning system (Philips Healthcare, Best, Netherlands) using a 32-channel head coil at St George's Hospital, London, UK. Acquisition included T1-weighted and QDI protocols. T1-weighted volume images were acquired using a Turbo Field Echo (TFE) sequence (TE = 3.7 ms, TR = 8.1 ms, TI = 1010 ms, flip angle 8° with a field of view (FOV) 240 mm × 240 mm T1-weighted images were acquired on young, healthy controls with 128 sagittal slices and voxel resolution 1 mm × 1 mm × 1.25 mm in 6 min 1 s, and for patients with 193 sagittal slices with 1 mm isotropic resolution in 6 min 47 s. Patient MRI acquisition was performed as part of a multimodal MRI protocol.

2.3.1. Diffusion image acquisition and pre-processing

Our QDI protocol was developed to provide voxel resolutions similar to conventional clinical DWI and to take advantage of ultra-high b-value tissue contrast. The TR is sufficiently long to ensure that significant T1 effects are not present in dMRI for healthy or pathological brain tissue.

Whole brain axial dMRI were acquired using a diffusion-sensitized spin-echo planar imaging (EPI) sequence in enhanced gradient mode (80mTm^{-1} at a slew rate of 100 mT m^{-1} ms^{-1}). Fat suppression was achieved using Spectral Presaturation by Inversion Recovery (SPIR) and Slice Selection Gradient Reversal (SSGR). Scan parameters included: TE = 90 ms, TR = 6000 ms, δ = 23.5 ms, Δ = 43.9 ms, field of view (FOV) 210 mm × 210 mm with twenty-two 5 mm thick slices acquired at 2.3 mm × 2.3 mm × 5 mm resolution that was zero-filled (by use of the Fourier transform) to provide 1.5 mm × 1.5 mm × 5 mm voxels. A SENSE factor 2 and half scan factor 0.891 were applied to minimise echo-train length and overall acquisition time. QDI protocols acquired dMRI at b = 0, 1100 and 5000 s mm^{-2} and DKI protocols at b = 0, 1100 and 3000 s mm^{-2}. Images without diffusion-sensitisation (i.e. b = 0 s mm^{-2}) were acquired 8 times.

For all young, healthy participants, QDWI was acquired in 3 orthogonal diffusion gradient directions (acquisition time 84s). QDTI was acquired in 6 diffusion directions equally spaced on the hemisphere (acquisition time 120s) and 15 directions equally spaced on the hemisphere (acquisition time 228s). DKI was acquired using identical gradient directions to 15 direction QDTI data. QDWI and QDTI data were acquired twice in the same scan session for five of the young, healthy participants

(age 33 ± 7 years, 2 male, 3 female) to allow computation of QDI scan-rescan reproducibility. The patients were scanned using the 6 diffusion direction QDTI protocol.

All dMRI acquisitions were denoised using MRTrix (MRTrix version 3, http://www.mrtrix.org/) (Veraart et al., 2019) and simultaneously corrected for motion and eddy current distortions by co-registration to the b = 0 s mm^{-2} image using FSL (version 5.0.11, https://fsl.fmrib.ox.ac.uk/fsl/fslwiki/) (Andersson et al., 2016).

2.4. Quasi-diffusion image computation

No image smoothing was performed prior to parameter estimation. $D_{1,2}$ and α were estimated in each diffusion gradient direction on a voxel-by-voxel basis from Eq. (4) using a Levenberg-Marquardt algorithm (http://www.gnu.org/software/gsl). Data fitting was initialised at each image voxel with $D_{1,2} = 2.98 \times 10^{-3} mm^2 s^{-1}$ and α = 0.978. Normalised entropy requires a numerical computation of an integral between b = 0 s mm^{-2} and infinity. For practical analysis we computed normalised entropy in each diffusion gradient direction over N = 100 uniform steps in q-space from b = 0 s mm^{-2} to b = 1,000,000 s mm^{-2} (i.e. q = 0 mm^{-1} to 4772.74 mm^{-1} in steps of q = 47.73 mm^{-1}). Padé approximation was used to enable rapid estimation of the MLF and its derivatives (Atkinson and Osselran, 2011; Ingo et al., 2017). Fig. 2 shows QDI model fits to dMRI data within representative grey and white matter voxels. The grey matter voxel provided $D_{1,2} = 0.75 \times 10^{-3} \pm 0.03 \times 10^{-3} mm^2 s^{-1}$ and α = 0.92 ± 0.04, whereas greater variability was apparent in the white voxel for $D_{1,2}$ and α by diffusion direction, $D_{1,2} = 0.74 \times 10^{-3} \pm 0.37 \times 10^{-3} mm^2 s^{-1}$ and α = 0.78 ± 0.07.

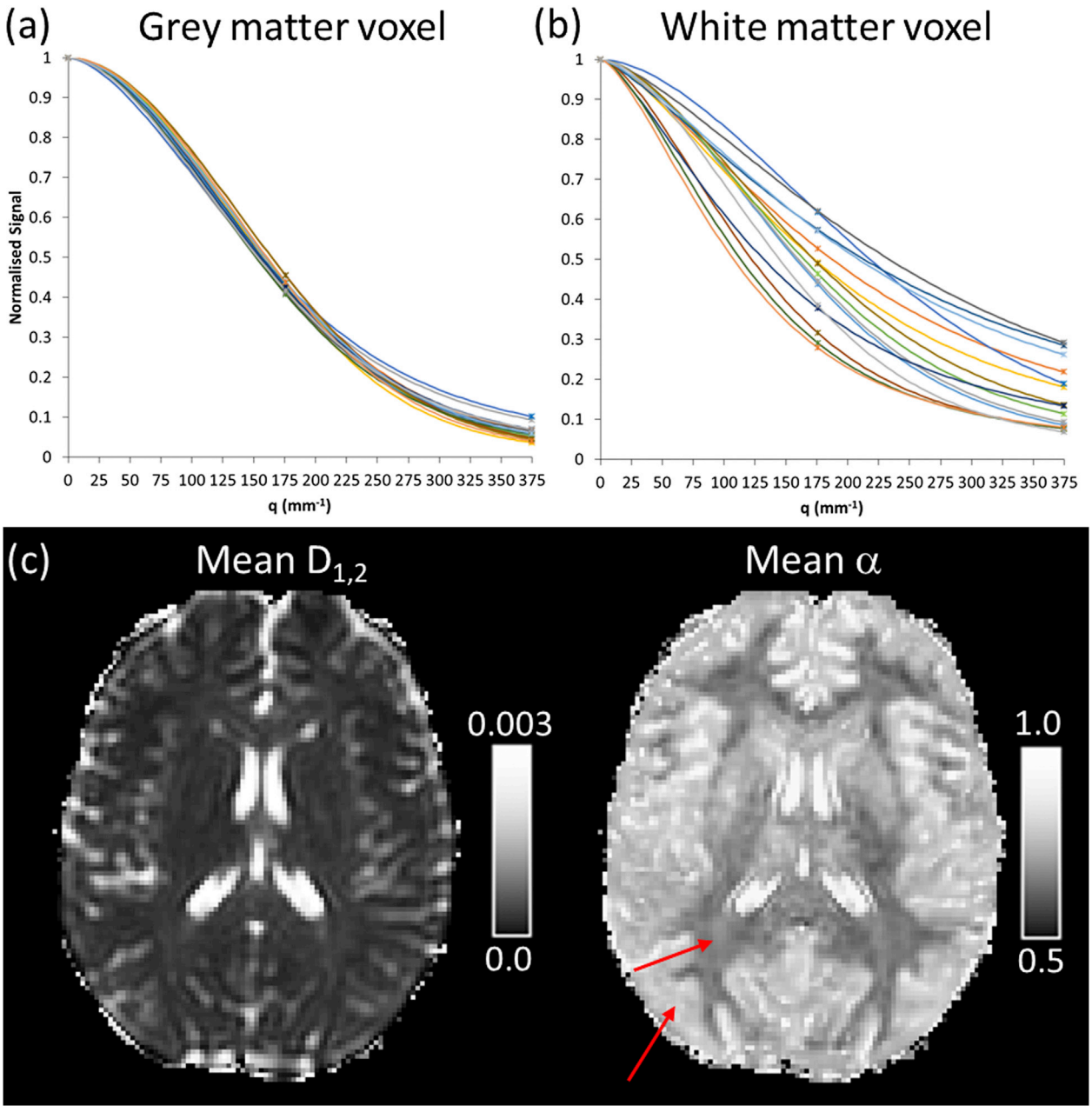

Fig. 2. QDI model fitting to dMRI data. QDI model fitting is illustrated for a young, healthy subject in application to the 15 diffusion gradient direction dMRI data. Data fits are shown for a representative grey matter (panel a) and white matter voxel (panel b) through q-space (in mm^{-1}). Voxel locations are indicated by the red arrows on mean $D_{1,2}$ and α maps (panel c) shown using the radiological convention.

QDWI and QDTI maps were computed as follows:

- **QDWI:** Each b-value shell was averaged prior to quasi-diffusion model fitting to provide mean $D_{1,2}$, α and H_n maps. These maps are quantitative but not rotationally invariant.
- **QDTI:** Quasi-diffusion model fitting was performed in each diffusion direction and rotationally invariant quantitative mean, axial, radial and anisotropy maps were computed from $D_{1,2}$, α and H_n tensors.

2.5. Computation of diffusional kurtosis

No data smoothing was performed prior to computation of DKI metrics. The diffusional kurtosis model was fitted to the diffusion signal attenuation across 15 diffusion gradient directions (b = 0, 1100, 3000 s mm^{-2}) using ExploreDTI (http://exploredti.com/) which uses the Robust Extraction of Kurtosis INDices with Linear Estimation (REKINDLE) approach (Tax et al., 2019). Mean, axial, radial and anisotropy maps were computed for the diffusion coefficient, D_κ, and kurtosis, κ.

2.6. Computation of tissue measures within healthy subjects

To allow assessment of QDI diffusion measures within specific brain tissues the T1-weighted images of the healthy volunteers were segmented into grey matter, white matter and CSF maps using New Segment in SPM (SPM version 12) (Ashburner and Friston, 2005) and the lateral ventricles using Freesurfer (Freesurfer version 5.3, https://surfer.nmr.mgh.harvard.edu/) (Fischl, 2012). The b = 0 s mm^{-2} images were aligned to the T1-weighted images using epi_reg in FSL (Greve and Fischl, 2009) and the resulting affine transformation was inverted to align T1-weighted images and anatomical ROIs to the dMRI data. To ensure tissue means, μ, and standard deviations, σ, were minimally affected by partial volume effects the tissue segmentations were thresholded at a probability of 0.9. Mean, axial, radial and anisotropy measures were computed for $D_{1,2}$, α, H_n, D_κ and κ in grey matter, white matter and lateral ventricle CSF. All voxels with $\kappa < 0$ or $\kappa > 3$ were excluded from κ measures.

Coefficients of variation, $CV = \sigma/\mu$, were computed in grey and white matter for mean $D_{1,2}$, α and H_n maps. Tissue intensity contrast, t_c, was computed as follows,

$$t_c = \frac{|\mu_{white} - \mu_{grey}|}{\sqrt{\sigma^2_{white} + \sigma^2_{grey}}},$$

where higher t_c values indicate greater tissue contrast.

2.7. Scan-rescan reproducibility of QDI measures

Scan-rescan reproducibility was performed by computing QDI diffusion measures in grey and white matter for mean $D_{1,2}$, α, and H_n measures for the 15, 6 and 3 diffusion gradient directions acquisitions and for $D_{1,2}$, α, and H_n anisotropy measures for the 15 and 6 direction protocols. Mean values, μ, were computed separately for grey and white matter across both scan sessions. Mean difference between scan sessions (i.e. accuracy), δ, and 95% confidence limits (i.e. precision) were also computed for each tissue type.

The scan-rescan data acquired for the 15 diffusion gradient direction protocol was also used to determine the reproducibility of fitted QDI signal attenuation curves. χ^2 was used to provide a measure of difference between the scan (i.e. expected) and rescan (i.e. observed) fitted curves, and was computed across 50 b-values evenly spaced between b = 0 s mm^{-2} and b = 5000 s mm^{-2} (sampled from the parameterised QDI decay curves) at each voxel and along each individual diffusion gradient direction. The χ^2 difference was normalised by dividing by the number of samples. As the distribution of χ^2 values did not follow a normal distribution the median, quartiles and 95th percentile were computed for each subject.

2.8. Statistical analysis

Spearman's rank correlation coefficients were used to investigate the relationship between mean tissue QDI measures with the hypotheses that $D_{1,2}$ and α represent different properties of the diffusion, and that $D_{1,2}$ and α are related to the composite H_n measure. The hypothesis that QDI and DKI measures are related was also tested between $D_{1,2}$ and D_κ, α and κ, and H_n and κ. Wilcoxon signed-rank tests were used to investigate differences between similar measures (n.b. diffusion coefficients, anisotropy and t_c measures) and were considered significant at $p < 0.05$.

2.9. Data and code availability statement

De-identified study data are available on request. The code is not available as it is subject to patent filing and commercialisation.

3. Results

3.1. QDI measures in healthy subjects

QDTI $D_{1,2}$, α and H_n maps acquired using the 15 direction dMRI protocol are shown in Fig. 3 with brain tissue means and standard deviations presented in Table 1.

3.1.1. $D_{1,2}$ and α maps

Mean, axial, radial and anisotropy $D_{1,2}$, maps (Fig. 3a & Table 1) exhibited conventional DTI tissue contrast. $D_{1,2}$ metrics had similar magnitudes to conventional DTI (Table 1) and were heterogeneous within brain tissue as indicated by high coefficients of variation and low tissue contrast between grey and white matter. In contrast, α maps (Fig. 3b & Table 1) provide information pertaining to properties of the diffusion dynamics within brain tissue. Diffusion dynamics within lateral ventricle CSF were Gaussian (mean α: 0.99 ± 0.01) with non-Gaussian diffusion in grey matter (mean α: 0.88 ± 0.01) and the greatest deviation from Gaussianity in white matter (mean α: 0.77 ± 0.01). Axial α values exhibited diffusion dynamics closer to Gaussianity than radial α values (Table 1). α anisotropy was smaller in magnitude than $D_{1,2}$ anisotropy (e.g. white matter: $D_{1,2}$ 0.60 ± 0.03; α 0.13 ± 0.01) and was significantly smaller in brain tissue (grey and white matter, $p = 0.008$).

Mean, axial and radial α maps had greater tissue intensity homogeneity than $D_{1,2}$ maps as indicated by low coefficients of variation (e.g. mean α: CV_{grey} 6.13 ± 0.46%, CV_{white} 6.92 ± 0.80%) and high t_c measures (e.g. mean α: t_c 1.45 ± 0.14). t_c was significantly greater in mean, axial and radial α maps than $D_{1,2}$ maps ($p = 0.008$ for each measure). Conversely, tissue contrast was greater in $D_{1,2}$ anisotropy ($p = 0.008$). Spearman's rank correlation coefficients indicated that, $D_{1,2}$ and α represent different aspects of the diffusion signal, with no significant relationships in grey and white matter between the metrics ($p > 0.05$). In general, $D_{1,2}$ and α tensor metrics were moderately to weakly related ($\rho < 0.43$) with high correlation in white matter radial measures only ($\rho = 0.69$, $p = 0.058$).

3.1.2. Normalised entropy

QDTI H_n maps (Fig. 3c & Table 1) provide a composite measure representing the diffusion signal attenuation curve. Lowest values of H_n were found in CSF (mean H_n: 0.32 ± 0.01), with greater values in grey matter (mean H_n: 0.49 ± 0.01) and highest values in white matter (mean H_n: 0.62 ± 0.01). Axial H_n measures were lower than radial values (Table 1). H_n anisotropy measures were significantly lower than $D_{1,2}$ and higher than α anisotropy in grey and white matter ($p = 0.008$).

Tissue H_n values were homogeneous (e.g. mean H_n: CV_{grey} 9.66 ± 0.79%, CV_{white} 7.51 ± 0.75%) and provided high tissue contrast (e.g. mean H_n: t_c 1.99 ± 0.18). Tissue contrast was greater in mean, axial and radial H_n maps than $D_{1,2}$ maps ($p = 0.008$ for each measure) and was

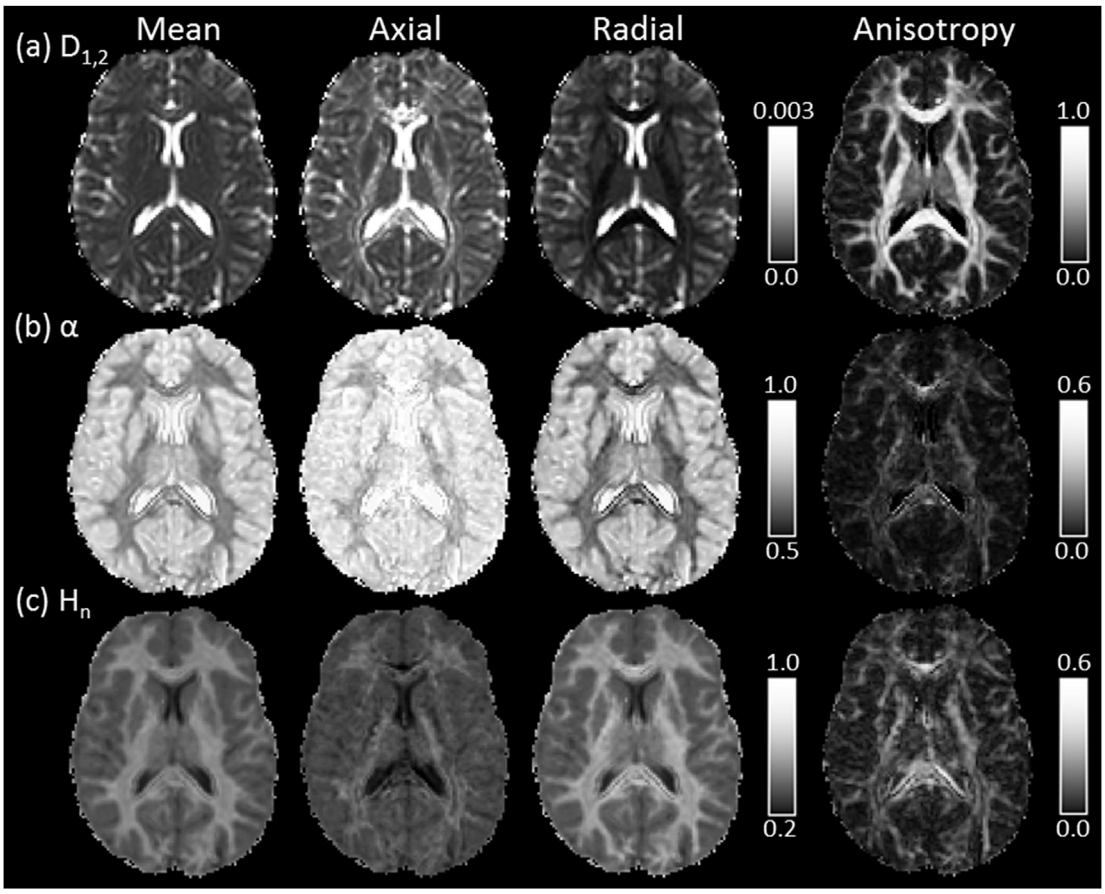

Fig. 3. QDTI data of a young, healthy subject for the 15 diffusion gradient direction acquisition (b = 0, 1100, 5000 s mm^{-2}, acquisition time 228 s). Mean, axial, radial and anisotropy maps are shown for row (a) $D_{1,2}$, (b) α and (c) H_n. Axial images are shown using the radiological convention.

significantly greater in mean and radial ($p = 0.008$), but not axial α maps ($p = 0.109$). Furthermore, H_n anisotropy maps had significantly lower t_c than $D_{1,2}$ anisotropy maps ($p = 0.008$) and higher t_c than α anisotropy ($p = 0.039$). Spearman's correlation coefficients indicate that, in general, H_n is more related to α than $D_{1,2}$. Specifically, $D_{1,2}$ and H_n were highly correlated in white matter radial measures (ρ = -0.69, p = 0.058), but all other tensor metrics exhibited weak to moderate correlations ($|\rho| < 0.595$). In contrast, α and H_n were highly correlated ($p < 0.05$) in all tensor metrics (grey matter: mean $\rho = -0.90$, axial ρ = -0.79, radial $\rho = 0.95$, anisotropy $\rho = 0.86$; white matter: mean $\rho = -0.71$, radial $\rho = -1.00$, anisotropy $\rho = 0.83$) except white matter axial diffusivity ($\rho = -0.381$). Together these results indicate that H_n values are weighted towards the α measure.

3.2. Comparison of QDI and DKI measures in healthy subjects

This section compares $D_{1,2}$ and D_κ, and α and κ measures computed from the 15 direction dMRI data. Table 1 presents brain tissue means and standard deviations for D_κ and κ in healthy subjects. Mean axial, radial and anisotropy κ maps are illustrated in Fig. 4a.

3.2.1. Relationship between $D_{1,2}$ and D_κ

Diffusivities calculated by the DKI technique were significantly greater than those computed by QDTI in grey and white matter tissue ($p = 0.008$ for mean, axial, and radial diffusivities) except for white matter axial diffusivity ($p = 0.547$). In addition, significantly greater anisotropy was observed in $D_{1,2}$ maps compared to D_κ in grey and white matter ($p = 0.008$). Tissue contrast was greater in $D_{1,2}$ than D_κ maps and showed significant differences in mean ($p = 0.039$), radial ($p = 0.008$) and anisotropy ($p = 0.008$) maps but not axial diffusivity ($p = 0.148$). Spearman's correlation coefficients indicated that $D_{1,2}$ and D_κ tensor metrics were positively correlated and significant ($p < 0.05$) in grey matter for mean $\rho = 0.91$, axial $\rho = 0.81$, and radial $\rho = 0.87$ measures and white matter for radial diffusivity ($\rho = 0.76$) all other measures were highly correlated ($0.548 < \rho < 0.595$).

3.2.2. Relationship between α and κ

Mean, axial and radial α maps (Fig. 3b & Table 1) exhibited inverted tissue intensities to κ (Fig. 4a & Table 1) in grey matter (e.g. mean α 0.88 ± 0.01; mean κ 0.58 ± 0.02), white matter (e.g. mean α 0.77 ± 0.01; mean κ 0.92 ± 0.03) and CSF (e.g. mean α 0.99 ± 0.01; mean κ 0.33 ± 0.02). Anisotropy values were significantly greater in κ than α maps in grey and white matter ($p = 0.008$). All tissue κ values were in agreement with previous DKI studies of brain tissue (Jensen et al., 2005; Jensen and Helpern, 2010).

Tissue contrast was not significantly different between mean or radial α and κ maps ($p > 0.05$) but was significantly greater in axial α than κ maps ($p = 0.008$). Anisotropy tissue contrast was significantly greater in κ than α maps ($p = 0.008$). Spearman's correlation coefficients indicate that α and κ tensor metrics are, in general, significantly negatively correlated (p < 0.05, grey matter: mean $\rho = -0.74$; axial ρ = -0.79; radial ρ = -0.79; white matter: radial $\rho = -0.76$; anisotropy $\rho = 0.79$). There was moderate to high correlation between α and κ in grey matter anisotropy ($\rho = 0.62$) and white matter mean ($\rho = 0.48$) and axial measures ($\rho = 0.57$).

3.2.3. Relationship between entropy and κ

Fig. 4 shows mean, axial, radial and anisotropy maps of κ (Fig. 4a) and H_n (Fig. 4b) in a healthy subject. Brain tissue means and standard deviations are presented in Table 1. All maps and tissue values are

Table 1
Mean (μ) and standard deviation (σ) values computed from QDI and DKI data for healthy grey matter, white matter and lateral ventricle cerebrospinal fluid (n = 8, age 29 ± 8 years). Measurements were computed from the 15 diffusion gradient direction dMRI data. Mean, axial, radial and anisotropy measurements are presented for $D_{1,2}$, α and H_n for QDI, and D_κ and κ for DKI.

		Grey Matter	White Matter	Cerebrospinal Fluid
		(μ±σ)	(μ±σ)	(μ±σ)
$D_{1,2}$ ($mm^2\ s^{-1}$)	Mean ($\times 10^{-3}$)	0.874 ± 0.036	0.701 ± 0.020	2.960 ± 0.028
	Axial ($\times 10^{-3}$)	1.032 ± 0.040	1.265 ± 0.043	3.000 ± 0.001
	Radial ($\times 10^{-3}$)	0.796 ± 0.035	0.420 ± 0.024	2.941 ± 0.043
	Anisotropy	0.173 ± 0.007	0.602 ± 0.026	0.018 ± 0.013
α	Mean	0.878 ± 0.004	0.769 ± 0.005	0.985 ± 0.002
	Axial	0.935 ± 0.005	0.868 ± 0.010	0.993 ± 0.006
	Radial	0.850 ± 0.005	0.720 ± 0.008	0.981 ± 0.005
	Anisotropy	0.069 ± 0.004	0.131 ± 0.013	0.010 ± 0.008
H_n	Mean	0.489 ± 0.006	0.621 ± 0.007	0.316 ± 0.016
	Axial	0.433 ± 0.006	0.502 ± 0.006	0.272 ± 0.010
	Radial	0.517 ± 0.007	0.680 ± 0.009	0.337 ± 0.021
	Anisotropy	0.113 ± 0.006	0.179 ± 0.009	0.134 ± 0.027
D_k ($mm^2\ s^{-1}$)	Mean ($\times 10^{-3}$)	0.962 ± 0.049	0.820 ± 0.021	3.680 ± 0.307
	Axial ($\times 10^{-3}$)	1.107 ± 0.051	1.276 ± 0.025	4.160 ± 0.388
	Radial ($\times 10^{-3}$)	0.888 ± 0.048	0.592 ± 0.025	3.440 ± 0.267
	Anisotropy	0.162 ± 0.010	0.472 ± 0.021	0.125 ± 0.015
κ	Mean	0.575 ± 0.020	0.923 ± 0.025	0.332 ± 0.020
	Axial	0.593 ± 0.020	0.736 ± 0.016	0.308 ± 0.016
	Radial	0.589 ± 0.017	1.181 ± 0.038	0.346 ± 0.024
	Anisotropy	0.126 ± 0.006	0.302 ± 0.021	0.024 ± 0.004

computed from the 15 direction dMRI data. Highest H_n and κ values were in white matter (e.g. mean H_n 0.62 ± 0.01; mean κ 0.92 ± 0.03) with lower values in grey matter (e.g. mean H_n 0.49 ± 0.01; mean κ 0.58 ± 0.02) and CSF (e.g. mean H_n 0.32 ± 0.02; mean κ 0.33 ± 0.02). κ anisotropy values were significantly greater than H_n anisotropy in grey and white matter ($p = 0.008$). H_n and κ tensor metrics were, in general, significantly positively correlated (grey matter: mean $\rho = 0.86$, axial $\rho = 0.81$, radial $\rho = 0.88$; white matter: mean $\rho = 0.88$; radial $\rho = 0.76$) or highly correlated in anisotropy measures (grey matter $\rho = 0.60$, white matter $\rho = 0.62$) with moderate correlations in white matter axial measures ($\rho = 0.33$). H_n maps had greater tissue intensity homogeneity than κ maps as indicated by lower coefficients of variation and significantly greater tissue contrast in mean, axial and radial maps ($p = 0.008$) except for anisotropy where greater tissue contrast was observed for κ ($p = 0.008$).

Brain tissue voxels that exhibit poor diffusional kurtosis model fitting (i.e. $\kappa < 0$ and $\kappa > 3$) were prevalent in κ maps and are represented by black voxels in Fig. 4a. Fitting errors occurred in 7.46 ± 1.29% of the total brain volume, with negative kurtosis values contributing to 99.40 ± 0.55% of this error. The QDI model was adequately fitted in these voxels (Fig. 4b).

3.3. Effect of reducing the number of diffusion gradient directions on QDI data

Fig. 5 shows mean $D_{1,2}$ (Fig. 5a) and H_n (Fig. 5b) maps for 15, 6 and 3 direction dMRI. Table 2 presents tissue means, voxel intensity standard deviations, coefficients of variation and tissue contrast measures for mean $D_{1,2}$, α and H_n maps. Acquisition times as a percentage of the 15 direction dMRI protocol were: 62.63% for 6 directions and 36.84% for 3 directions. Reducing the number of diffusion gradient directions caused a small decrease in mean tissue $D_{1,2}$ and α values, and an increase in H_n (Table 2). For 15 vs 6 diffusion directions these differences were not significant ($p > 0.05$), but for 15 vs 3 directions significant differences were found in $D_{1,2}$, α and H_n values in grey and white matter ($p = 0.008$), potentially due to the lack of rotational invariance of the QDWI (i.e. 3 diffusion direction) measures when compared to QDTI data. There were no significant differences in tissue contrast for 15 vs 6 directions ($p > 0.05$), but there were significant differences for 15 vs 3 directions in $D_{1,2}$, α and H_n ($p = 0.001$). All H_n maps showed significantly greater tissue contrast when compared to κ maps (H_n vs κ: 15 directions $p = 0.008$; 6 directions $p = 0.008$; 3 directions $p = 0.016$), but no significant differences were found for α compared to κ (15 directions $p = 1.00$; 6 directions $p = 0.250$) except for 15 vs 3 ($p = 0.008$ with κ contrast greater than α.

3.4. Reproducibility of QDI measures

Scan-rescan reproducibility results are presented in Table 3. Reproducibility was good for all mean QDI measures as indicated by mean percentage error ($E = 100 \times \delta/\mu$) less than ±0.75% in grey and white matter for $D_{1,2}$, α and H_n for each of the 3, 6 and 15 diffusion gradient direction acquisitions. Accuracy and precision of measurements were improved, and mean percentage error was reduced by increasing the numbers of acquired diffusion directions. This effect was greater in white than grey matter. Anisotropy measures showed lower accuracy and precision than mean QDI measures. Increasing the number of diffusion directions improved accuracy and precision of anisotropy measurements. Mean percentage error was less than ±0.5% for $D_{1,2}$ anisotropy in both grey and white matter, but was greater for α and H_n anisotropy measures (e.g. 6 directions: α anisotropy $E_{grey} = 4.07\%$, $E_{white} = 2.74\%$; H_n anisotropy $E_{grey} = 3.74\%$, $E_{white} = 1.17\%$) and was improved by increasing the number of diffusion gradient directions (15 directions: α anisotropy $E_{grey} = 1.13\%$, $E_{white} = 0.23\%$; H_n anisotropy $E_{grey} = 1.26\%$, $E_{white} = -0.14\%$).

Reproducibility of fitted QDI diffusion signal attenuation curves was high in both grey (χ^2: LQ 0.0006 ± 0.0003; median 0.0017 ± 0.0009; UQ 0.0047 ± 0.0028; 95th percentile 0.0312 ± 0.0250) and white matter (χ^2: LQ 0.0005 ± 0.0001; median 0.0016 ± 0.0004; UQ 0.0041 ± 0.0015; 95th percentile 0.0262 ± 0.0189). χ^2 values were similar in grey and white matter indicating that there is not a tissue specific bias in reproducibility.

3.5. Application of QDI to patient cases

Case studies of two SVD patients (Fig. 6) and three brain tumour patients (Fig. 7) are described in the following section. QDI was acquired using the 6 direction QDTI protocol in 120s. Mean $D_{1,2}$, α and H_n maps

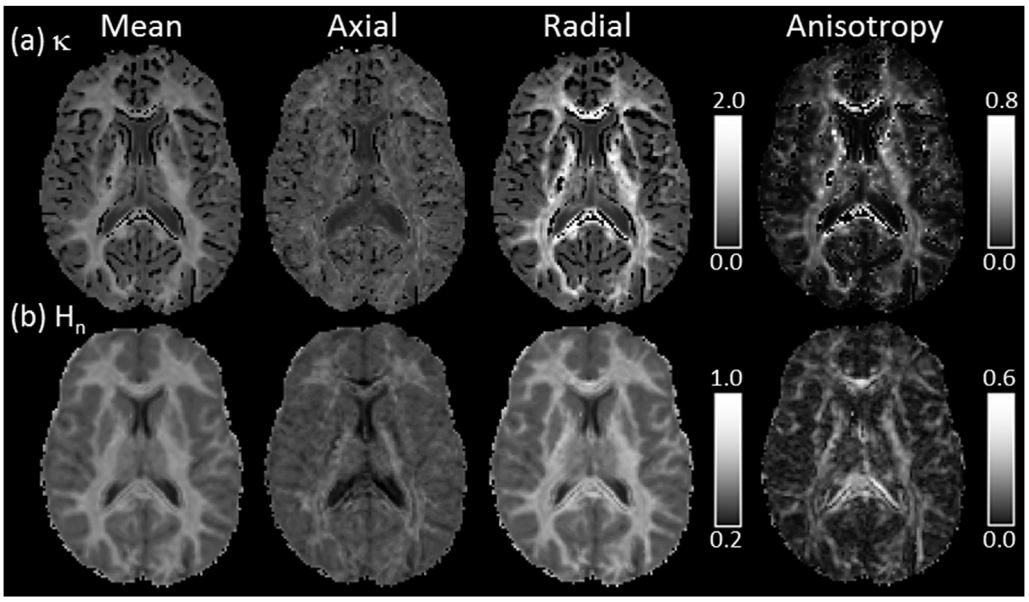

Fig. 4. Comparison of mean, axial, radial and anisotropy maps computed by QDTI (on b = 0, 1100, 5000 s mm^{-2}) and DKI (on b = 0, 1100, 3000 s mm^{-2}) for the 15 diffusion gradient direction acquisition (acquisition time 228 s). Axial images are shown for κ (row a) and H_n maps (row b). All images are shown using the radiological convention for a young, healthy subject.

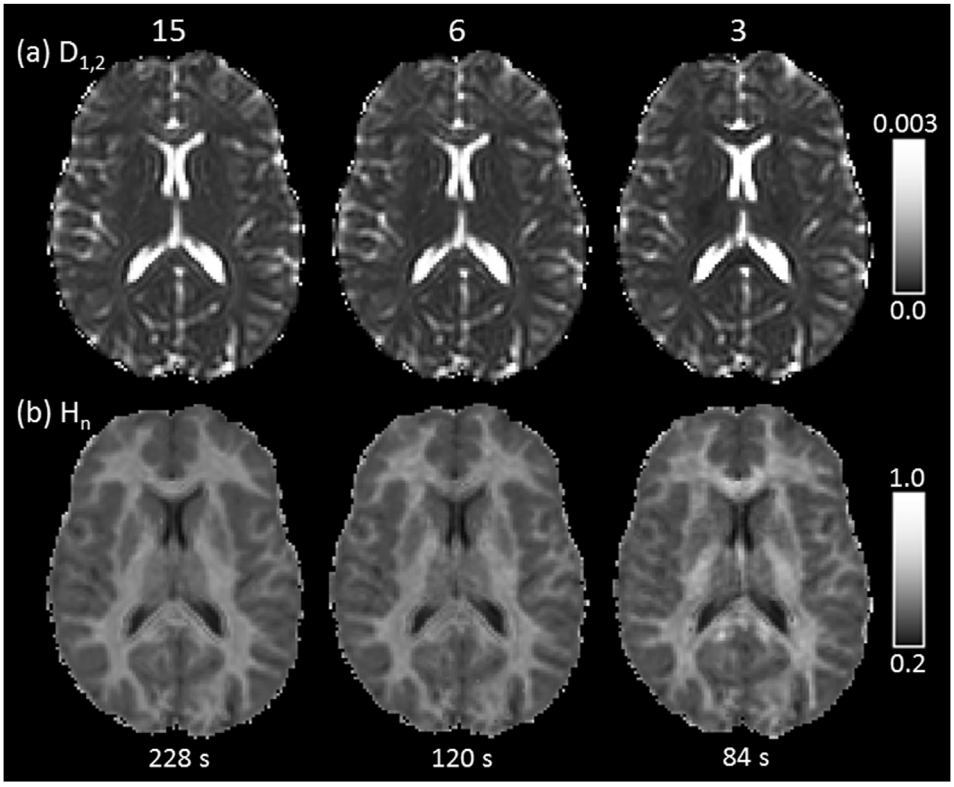

Fig. 5. Comparison of QDI maps computed using different numbers of diffusion gradient directions. From left to right the numbers of gradients are 15 (acquisition time 228 s), 6 (acquisition time 120 s) and 3 (acquisition time 84 s). Row (a) shows mean $D_{1,2}$ maps and row (b) shows mean H_n maps. All images are shown using the radiological convention for a young, healthy subject.

are shown with $D_{1,2}$ anisotropy in Fig. 6, and direction encoded colour maps (Pajevic and Pierpaoli, 1999) in Fig. 7.

Fig. 6a shows a SVD patient with periventricular white matter lesions (WML) and enlarged ventricles. WML exhibited higher $D_{1,2}$, and included regions of reduced $D_{1,2}$ anisotropy and H_n and elevated α (yellow arrows). The α and H_n maps indicate that diffusion dynamics are closer to Gaussian and that WML tissue microstructure is less complex and more damaged than healthy white matter. Regions of elevated α and reduced H_n extend into normal appearing white matter beyond regions of high mean $D_{1,2}$ and reduced $D_{1,2}$ anisotropy. This effect was more apparent in α than H_n maps. Fig. 6b shows a SVD patient with an incidental acute ischaemic infarct in the left thalamus and posterior limb of the internal

Table 2
Mean (μ), standard deviation (σ), coefficients of variation (CV) and tissue contrast measurements for healthy grey and white matter tissue in QDI and DKI data (n = 8, age 29 ± 8 years). Measurements are computed from dMRI data acquisitions with 3, 6 and 15 diffusion gradient directions for maps of mean $D_{1,2}$, mean α, mean H_n and mean κ. All measures are presented as mean ± standard deviation.

Gradient directions		3	6	15
$D_{1,2}$(mm^2 s^{-1})	μ_{grey} (× 10^{-3})	0.863 ± 0.036	0.868 ± 0.033	0.874 ± 0.036
	σ_{grey} (× 10^{-3})	0.338 ± 0.044	0.330 ± 0.046	0.331 ± 0.049
	CV_{grey} (%)	39.106 ± 4.116	37.958 ± 4.351	37.763 ± 4.567
	μ_{white} (× 10^{-3})	0.638 ± 0.029	0.695 ± 0.019	0.701 ± 0.020
	σ_{white} (× 10^{-3})	0.292 ± 0.052	0.248 ± 0.048	0.239 ± 0.046
	CV_{white} (%)	45.835 ± 8.128	35.665 ± 6.996	34.208 ± 6.847
	Tissue Contrast	0.506 ± 0.060	0.417 ± 0.059	0.442 ± 0.056
α	μ_{grey}	0.873 ± 0.006	0.877 ± 0.004	0.879 ± 0.004
	σ_{grey}	0.064 ± 0.007	0.056 ± 0.004	0.054 ± 0.004
	CV_{grey} (%)	7.289 ± 0.812	6.346 ± 0.495	6.126 ± 0.464
	μ_{white}	0.739 ± 0.005	0.768 ± 0.004	0.769 ± 0.005
	σ_{white}	0.080 ± 0.006	0.056 ± 0.006	0.053 ± 0.006
	CV_{white} (%)	10.983 ± 0.776	7.337 ± 0.818	6.920 ± 0.803
	Tissue Contrast	1.319 ± 0.151	1.392 ± 0.137	1.445 ± 0.140
H_n	μ_{grey}	0.495 ± 0.008	0.491 ± 0.005	0.489 ± 0.006
	σ_{grey}	0.055 ± 0.007	0.049 ± 0.004	0.047 ± 0.004
	CV_{grey} (%)	11.157 ± 1.224	9.918 ± 0.858	9.656 ± 0.789
	μ_{white}	0.653 ± 0.005	0.623 ± 0.005	0.621 ± 0.007
	σ_{white}	0.074 ± 0.005	0.049 ± 0.005	0.047 ± 0.005
	CV_{white} (%)	11.327 ± 0.694	7.890 ± 0.800	7.508 ± 0.750
	Tissue Contrast	1.731 ± 0.169	1.928 ± 0.167	1.990 ± 0.188
κ	μ_{grey}	–	–	0.575 ± 0.020
	σ_{grey}	–	–	0.158 ± 0.013
	CV_{grey} (%)	–	–	27.525 ± 2.420
	μ_{white}	–	–	0.923 ± 0.025
	σ_{white}	–	–	0.177 ± 0.018
	CV_{white} (%)	–	–	19.165 ± 1.991
	Tissue Contrast	–	–	1.472 ± 0.129

capsule (red arrows). The acute infarct exhibited low $D_{1,2}$ and α values, with high H_n values, corresponding to an increase in restriction of the diffusion environment.

Fig. 7 shows patients with a Grade I meningioma (Fig. 7a), a Grade II astrocytoma (Fig. 7b) and a Grade IV glioblastoma (Fig. 7c) with tumour cores (red arrows) and oedema (yellow arrows) indicated. The high-grade tumour core (i.e. glioblastoma) exhibited low $D_{1,2}$ and α, and high H_n, in regions corresponding to high tumour cellularity as indicated by blood brain barrier breakdown due to active tumour growth and the presence of neovascularisation (as shown by gadolinium contrast enhancement on T1-weighted images). This ring of viable tumour surrounds a necrotic region with high $D_{1,2}$ and α, and low H_n. Infiltrative oedema adjacent to the tumour core exhibited elevated $D_{1,2}$, higher α and lower H_n compared to healthy white matter. The more 'benign' tumour cores (i.e. meningioma, Fig. 7a, and low-grade astrocytoma, Fig. 7b) exhibited elevated $D_{1,2}$ and α and lower H_n values than healthy white matter, with H_n values greater than grey matter in meningioma and less than grey matter in astrocytoma. The astrocytoma core was characterised by high $D_{1,2}$ and α, and low H_n, and likely represents an infiltrative mix of tumour and normal brain tissue, as compared to the meningioma and high-grade cores that are more likely cellularly dense tumour tissue. Oedema surrounding the meningioma exhibited elevated $D_{1,2}$ and α and lower H_n compared to healthy white matter.

Table 3
Scan-rescan reproducibility of QDI measures in grey and white matter for mean and anisotropy measures for the 3, 6 and 15 diffusion direction protocols. Reproducibility of $D_{1,2}$, α and H_n measures is presented for mean and anisotropy metrics across 5 young, healthy subjects (n = 5, age 33 ± 7 years). Mean tissue values across both scan sessions, μ, are presented with mean difference between scan sessions (i.e. accuracy), δ, and 95% confidence limits (i.e. precision) for each tissue type.

	Number of directions	μ_{grey}	μ_{white}	δ_{grey} [95% confidence limits]	δ_{white} [95% confidence limits]
Mean					
$D_{1,2}$ (× 10^{-3} mm^2s^{-1})	3	0.861	0.644	0.006 [-0.005, 0.018]	0.004 [-0.013, 0.021]
	6	0.867	0.700	−0.000 [-0.013, 0.013]	−0.000 [0.024, 0.024]
	15	0.869	0.705	0.002 [-0.009, 0.014]	−0.002 [0.009, 0.005]
α	3	0.866	0.742	−0.003 [-0.008, 0.001]	−0.002 [-0.012, 0.008]
	6	0.872	0.767	−0.001 [-0.005, 0.003]	0.001 [-0.008, 0.010]
	15	0.872	0.768	−0.001 [-0.003, 0.002]	0.000 [-0.002, 0.003]
H_n	3	0.502	0.650	0.002 [-0.001, 0.005]	0.001 [-0.007, 0.008]
	6	0.496	0.623	0.001 [-0.004, 0.006]	−0.001 [-0.008, 0.005]
	15	0.496	0.621	0.000 [-0.001, 0.002]	0.000 [-0.003, 0.002]
Anisotropy					
$D_{1,2}$	6	0.200	0.591	0.000 [-0.020, 0.021]	0.001 [-0.009, 0.011]
	15	0.183	0.583	−0.001 [-0.004, 0.002]	−0.001 [-0.003, 0.001]
α	6	0.084	0.168	0.003 [-0.008, 0.015]	0.005 [-0.009, 0.018]
	15	0.070	0.130	0.001 [-0.003, 0.005]	0.000 [-0.006, 0.007]
H_n	6	0.131	0.221	0.005 [-0.007, 0.017]	0.003 [-0.007, 0.012]
	15	0.112	0.178	0.001 [-0.005, 0.008]	0.000 [-0.006, 0.005]

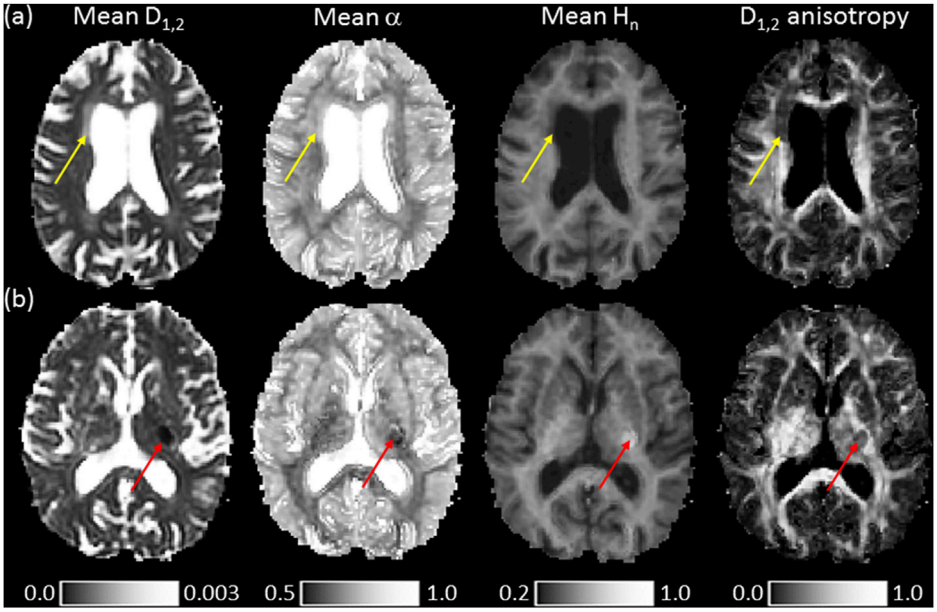

Fig. 6. Application of QDTI to a patient with small vessel disease (row a), and a patient with an acute ischemic infarct (row b). Mean maps of $D_{1,2}$, α and H_n are shown with. $D_{1,2}$ anisotropy. All axial images are shown using the radiological convention and were acquired using the 6 diffusion gradient direction QDTI sequence (acquisition time 120 s). Yellow arrows indicate the location of periventricular white matter lesions (row a) and red arrows show the location of the acute ischemic infarct (row b).

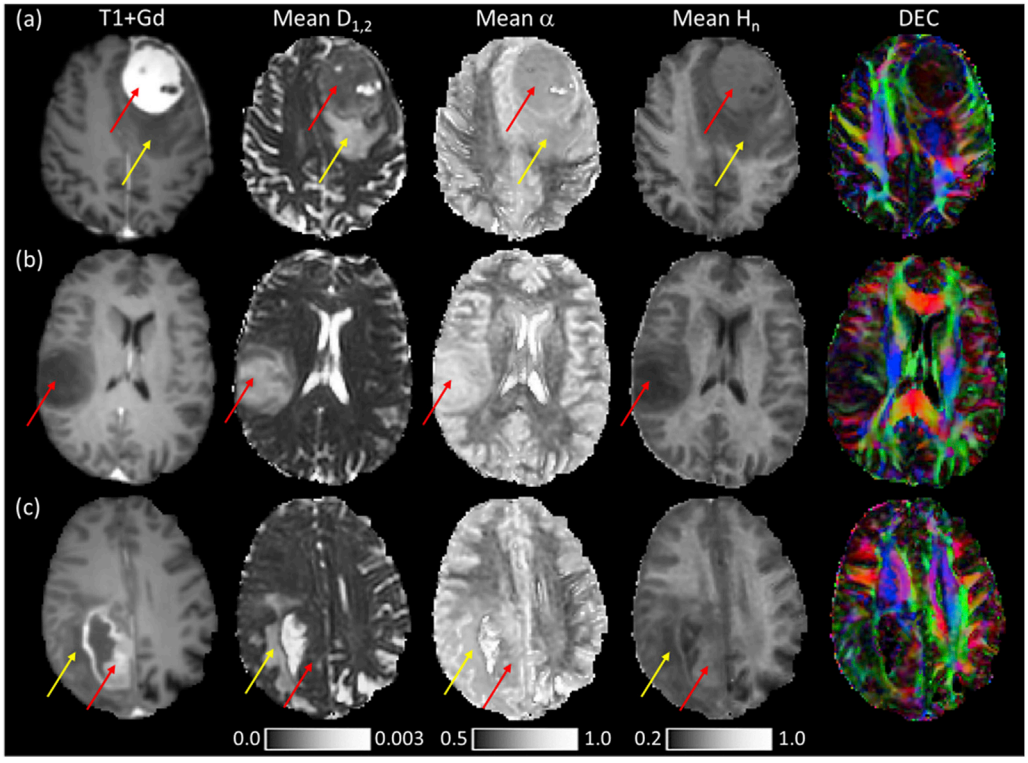

Fig. 7. Application of QDTI to patients with brain tumour. Row (a) shows a Grade I meningioma, row (b) a Grade II astrocytoma and row (c) a Grade IV glioblastoma. Mean maps of $D_{1,2}$, α and H_n are shown with Direction Encoded Colour maps (DEC) that are modulated by $D_{1,2}$ anisotropy. The DECs are computed from the principal eigenvector of the $D_{1,2}$ tensor map and represent the gross orientation of brain tissue within a voxel (red – left/right, green – anterior/posterior, blue superior/inferior). All axial images are shown using the radiological convention and were acquired using the 6 diffusion gradient direction QDTI sequence (acquisition time 120 s). Red arrows indicate the location of the tumour cores and yellow arrows show the location of oedematous regions.

4. Discussion

We have described a new quantitative dMRI method, QDI that is based on a special case of the CTRW model and describes non-Gaussian diffusion. This method may be applied to diffusion signal attenuation within a voxel and can be used to estimate the rate of diffusion, $D_{1,2}$, and the shape of the diffusion signal decay curve, α. Our QDI method also overcomes several limitations of DKI. QDI can be used to generate maps analogous to k (i.e. α and H_n) and can be added to existing single b-value shell acquisition protocols by acquiring an additional high b-value along each diffusion gradient direction. We have shown that QDTI provides maps with high tissue contrast and allows computation of mean, axial, radial and anisotropy maps. Acquisition of the maps utilises a rapid MR imaging protocol which may be implemented on standard clinical MRI systems in 84s for QDWI and 120s for QDTI. We have also shown that QDTI provides clinically meaningful tissue contrast.

4.1. Conceptualisation of the quasi-diffusion model in application to biological systems and MRI

The assumption of particle collision dynamics (i.e. the presence of waiting time and step length pdfs) in diffusion processes is a widespread

and standard notion. It is central to the standard model of Brownian motion (Einstein, 1905; Mazo, 2009) which assumes that particles remain stationary for sufficient time such that their next displacement is not correlated with the previous one. In such models the particle displacements are instantaneous. The interpretation of this mathematical assumption is either that a series of observations are made at fixed time increments, or that a large number of collisions with other particles are required to displace the diffusing particle. The difference between the CTRW approach and conventional Brownian motion lies in the distributions of step lengths and waiting times that are assumed. For Brownian motion, these are assumed to be distributed with a well-defined mean, which is considered to be a fixed increment in the simplest treatises (Mazo, 2009), but any waiting time distribution with a well-defined mean will lead to ordinary (i.e. Brownian) diffusion dynamics in some time regime. The CTRW model allows a generalisation of possible diffusion dynamics by not assuming that waiting time and step length pdfs are Gaussian. We acknowledge that this is an assumption, but it is a very general assumption with a well-studied mathematical basis and includes ordinary Gaussian diffusion as a limiting case.

Translating fractional diffusion models of CTRW processes to scientific applications is challenging (Metzler et al., 2014). The mathematics of fractional diffusion equations represent a generalisation of the diffusion equation (Mainardi et al., 2001) but often it is not clear which types of fractional equations should be applied as mathematical models of particular physical phenomena. A limitation of the QDI technique is that we do not have empirical evidence of quasi-diffusion processes within biological tissue. Nevertheless, there are several good reasons for use of the quasi-diffusion special case, $\beta = 2\alpha$, of the fractional diffusion equations in dMRI. Firstly, the quasi-diffusion case assumes that the ensemble average of diffusing spins within a voxel has mean-squared displacement proportional to linear time. This assumption ensures that QDI models non-Gaussian diffusion dynamics using the same spatial and temporal scaling relationship as for ordinary diffusion (i.e. where $\alpha = 1$ and $\beta = 2$ and $2\alpha/\beta = 1$), a side effect of which it is possible to estimate the diffusion coefficient, $D_{1,2}$, in conventional units of mm^2s^{-1}. Secondly, this assumption ensures that super- and sub-diffusive dynamics are not considered within the model causing diffusion dynamics to be anomalous for $\alpha \neq 1$ but not exotic. Instead QDI allows an extension of ordinary diffusion at $\alpha = 1$ to non-Gaussian but Brownian-like diffusion dynamics when $0 < \alpha < 1$. Finally, the diffusion dynamics of the QDI model may be interpreted with respect to mathematical results pertaining to the fundamental solution of the space-time fractional diffusion equations (Mainardi et al., 2001) in the QDI case (Luchko, 2016, 2019) which is referred to as α-fractional diffusion by Luchko. For the QDI case, the diffusion propagator is a Gaussian-like function which becomes Gaussian when $\alpha = 1$ (Luchko, 2016, 2019). Furthermore, the entropy production rate of the propagator is independent of α, and identical to ordinary diffusion (Luchko, 2016). Together these results suggest that QDI may be considered a "natural fractionalisation" (Luchko, 2016) of ordinary diffusion and that it represents a model of quasi-Brownian diffusion, hence the moniker Quasi-Diffusion Imaging.

The quasi-diffusion model has several advantages over the general CTRW model in application to dMRI data. Firstly, QDI requires a considerably reduced imaging protocol compared to the general CTRW model (e.g. Karaman et al., 2016). Our coupling of fractional exponents allows data acquisition across q-space alone and represents a pragmatic, clinically feasible solution to ensuring acquisition times are short as there is not a requirement to estimate α and β independently. Secondly, QDI assumes regular scaling in time and space and allows estimation of non-Gaussian diffusion within a voxel and similar inference of the underlying tissue microstructural environment to DKI. Finally, the QDI technique provides a diffusion coefficient in conventional units of mm^2s^{-1}. This is advantageous over the CTRW model as estimation of additional measures to allow recovery of units from $mm^{\beta}s^{-\alpha}$ (Ingo et al., 2014b; Karaman et al., 2016; Magin et al., 2013, 2019) are not required. Overall the QDI technique has advantages in parameter inference, improves stability of model fitting and allows rapid dMRI acquisition with good tissue contrast.

Conceptually, quasi-diffusion is a model of transport (i.e. diffusion dynamics) that describes the dMRI signal and is not based on a model of tissue microstructure. Consequently, QDI does not have the problems that are associated with microstructural assumptions in dMRI, such as acquisition and parameter-based bias (Jelescu et al., 2015; Jelescu and Budde, 2017), and model degeneracy (Jelescu et al., 2015) that cannot always be adequately resolved (Novikov et al., 2018b). In dMRI the quasi-diffusion model may be interpreted as approximating the action of a heterogeneous environment on diffusing spins. Within a biological tissue the spin motion will involve interaction with other water molecules, larger molecular species, and the potential for binding and unbinding with cellular surfaces (i.e. trapping) and constitutes a large variety of mechanisms that contribute to the observed signal attenuation. The signal in dMRI is observed as an ensemble average within an image voxel inside which partial volumes cannot be reliably attributed to different spin dynamics. The power of QDI is in its simplicity and general applicability in defining the observed diffusion signal attenuation without the need for microstructural assumptions relating to separate contributions of different spin populations within a voxel. In this way QDI offers a simplified fitting to non-Gaussian diffusion signal attenuation and provides a reliable representation of the signal decay curve.

In this study we have shown the capabilities of this technique by acquiring dMRI data quickly to obtain high quality images analogous to DKI, whilst overcoming the inherent limitations of the DKI technique. QDI can be applied over any b-value range, does not require large numbers of diffusion gradient directions or make strong geometrical assumptions. It can be applied to any organ throughout the body to measure diffusion without theoretical modification and recalibration. Crucially, as the QDI technique offers a powerful alternative representation of signal decay it could be used within any dMRI application that requires reliable parameterisation of non-Gaussian signal attenuation.

4.2. Properties of Quasi-Diffusion Imaging maps

Diffusion coefficient maps computed from QDI have similar tissue contrast to conventional DWI and DTI. $D_{1,2}$ maps have lower magnitudes and higher anisotropy than DKI D_κ maps. Differences in magnitude between $D_{1,2}$ and D_κ metrics are similar to those observed after application of free water elimination techniques to conventional dMRI data (Albi et al., 2017; Pasternak et al., 2009). Our QDI technique exhibited greater differences in radial diffusivity (−30.1%) and anisotropy measures (+26.2%) and smaller differences in mean (−13.8%) and axial diffusivities (−0.4%). The similarity between our results and those of Albi et al. (2017) indicate that use of ultra-high b-values in QDI acquisition potentially reduces partial volume effects due to free water, however, it should be noted that changing $\overline{\Delta}$ in QDI acquisitions will alter measured diffusion coefficients (Topgaard, 2017).

QDI provides maps of α, a fractional exponent representing the shape of the diffusion signal attenuation within a voxel, which represents the deviation from Gaussianity of the diffusion process. Our findings indicate that diffusion in CSF is Gaussian, while grey matter and white matter are characterised by non-Gaussian diffusion properties. Greater non-Gaussian diffusion is indicated by a thicker power law tail of the diffusion signal attenuation and represents greater heterogeneity of the diffusion process. Our findings are in broad agreement with previous CTRW model studies (Karaman et al., 2016; Magin et al., 2013), but do not attempt to separate time and space exponents. In particular, lower α values in white matter than grey matter indicate that step lengths are shorter and waiting times longer, potentially due to greater heterogeneity of the cellular boundaries to diffusion in the tissue microstructural environment, and consequently greater hindrance or restriction to water diffusion at shorter length scales in well organised axons, myelin and oligodendrocytes.

We computed normalised entropy, H_n, from the parameterised diffusion signal decay curve to provide a composite measure of $D_{1,2}$ and α. The H_n measure provides information relating to the tissue microstructural environment as it calculates the information content of the diffusion signal attenuation over multiple length scales, and potentially represents a biomarker of tissue organization, structure and complexity (Ingo et al., 2014a, 2014b; Magin et al., 2013). Higher H_n values correspond to lower rates of diffusion and greater non-Gaussianity and heterogeneity of the diffusion dynamics, whereas lower H_n values correspond to higher rates of diffusion and more Gaussian diffusion dynamics (Ingo et al., 2014a, 2014b; Magin et al., 2013, 2019). Tissue contrast in H_n maps is analogous to DKI κ maps and has similar contrast to H_n maps in *ex vivo* rodent brain data (Ingo et al., 2014b). Our results indicate greater heterogeneity of the diffusion environment in white matter than grey matter, and consequently more complex diffusion dynamics. QDI H_n maps offer a potential alternative to κ maps, with similar interpretation, but significantly improved tissue contrast.

The $D_{1,2}$ and α parameters provided by QDI are quantitative, in the same way that DTI and DKI maps are quantitative. For QDI metrics to be comparable across studies and scanners it is necessary to acquire dMRI data with similar diffusion times (Topgaard, 2017). Furthermore, to ensure that H_n measures are reproducible and comparable across studies it is necessary to ensure that similar weightings of the $D_{1,2}$ and α parameters to normalised entropy are preserved. For instance, the normalised entropy should be computed over the same q- or b-value range using the same total number of samples taken along the diffusion signal attenuation curve.

QDI maps are rotationally invariant in the case of QDTI and the usual limitations of the tensor model are relevant for these images (e.g. Wheeler-Kingshott and Cercignani, 2009). A further limitation in QDI is that $D_{1,2}$ and α tensor maps are computed separately without a mathematical description that allows their simultaneous computation. This means that principal directions of α maps may not be precisely oriented along principal diffusion directions. An aim of future research will be to derive the mathematical form for the QDI tensor. We will also explore orientation distribution functions of QDI measures in high angular resolution dMRI and investigate their application to white matter tractography.

4.3. Advantages of Quasi-Diffusion Imaging over Diffusional Kurtosis Imaging

QDI has several advantages over DKI that improve accuracy of calculated measures and stability of model parameter estimates. Firstly, no data smoothing was performed in this study and initial parameter estimates were set to the same values in all voxels (specifically, $D_{1,2} = 2.98 \times 10^{-3}\text{mm}^2\text{s}^{-1}$ and $\alpha = 0.978$). Such an initialisation was possible as perturbation of initial conditions provided minimal change to estimated parameters, indicating robust model fitting in the presence of noise. This is further supported by the capability of QDI to provide: (a) model fitting along single lines through q-space, and (b) parameter estimation within voxels characterised by negative kurtosis estimates in DKI, a phenomenon attributed to low signal to noise ratios (Jensen and Helpern, 2010; Tabesh et al., 2011). Secondly, QDI can be used to predict diffusion signal attenuation at extremely high b-values, in contrast to DKI, a feature exploited in calculation of H_n. Finally, QDI enables diffusion sensitisation to be increased to the maximum capability of current and future MRI systems. This allows QDI to be applied to any b-value range given sufficient signal to noise ratios, and consequently takes advantage of additional tissue contrast provided by ultra-high b-values and its increased sensitivity to subtle changes in tissue ultrastructure. Recently, ultra-high b-value imaging has provided additional insight to diseases such as Alzheimer's disease (Yingnan et al., 2018), Parkinson's disease (Xueying et al., 2015) and brain tumour subtypes (Tan et al., 2018) but computation of diffusion metrics in these studies has been limited by a lack of analysis techniques embedded in a physical model for diffusion processes (e.g. Tan et al., 2018; Xueying et al., 2015; Yingnan et al., 2018). QDI provides a quantitative framework for analysing such data and computes physically meaningful metrics that may be used to provide additional insight to disease.

4.4. Clinical potential of Quasi-Diffusion Imaging

As QDI provides analogous information to DKI it is likely that the current wealth of findings from clinical DKI studies also represent potential clinical benefits of QDI. In particular, the potential clinical utility of QDI is in providing additional diagnostic or prognostic information beyond that of conventional DWI and DTI. We have shown that QDTI is sensitive to white matter damage beyond white matter lesions (identified by elevated $D_{1,2}$) in a SVD patient and showed that damaged tissue exhibited more Gaussian diffusion dynamics indicating a less complex tissue microstructural environment potentially caused by axonal degeneration, demyelination and gliosis. Numerous studies indicate that conventional DTI measures are sensitive to white matter damage in SVD (Raja et al., 2019) and Xu et al. (2016) report increases in D_κ and decreases in mean κ in normal appearing white matter that are proportional to disease severity. This indicates the added value of DKI beyond conventional DWI and suggests that QDI would provide increased sensitivity to white matter damage in SVD.

QDTI was also applied to a SVD patient with an incidental acute ischaemic infarct. QDTI reproduces the reduction of mean $D_{1,2}$ observed due to the effects of cytotoxic oedema (i.e. oncotic swelling of glial and neuronal cells reducing the extracellular space (von Kummer and Dzialowski, 2017)) in conventional DWI. Mean α and H_n was increased and provided clear delineation of the infarct. Observation of high mean H_n is analogous to DKI studies that report high mean κ in acute stroke lesions (Jensen, 2018; Yin et al., 2018; Zhu et al., 2019) which have been suggested to represent an increase in tissue complexity (Jensen, 2018). Preclinical DKI studies have shown that stroke lesions with a mismatch between reduced D_κ and increased κ indicate tissue with less severe ischemic injury than in lesions where reduced D_κ and increased κ overlap (Cheung et al., 2012; Lu et al., 2018) and consequently provide more information than conventional DWI. Furthermore, in a recent clinical DKI study, Yin et al. (2018) have shown that high mean κ within acute lesions indicates brain tissue that is identified as lesion on T2-weighted images at one month follow-up. As QDI and DKI are analogous, QDI potentially provides a rapid technique for identifying acute stroke lesions in the clinic and could include valuable information that is not provided by conventional DWI regarding patient recovery that could guide future therapeutic and intervention strategies.

QDTI showed low-grade glioma to exhibit diffusion properties indicative of increased tissue water content and presence of damaged tissue due to infiltrative tumour growth. In contrast, the high-grade tumour exhibited a ring of reduced $D_{1,2}$ and α, and increased H_n associated with viable tumour. In this case, high H_n regions likely represent higher tumour-cell density due to rapid growth, corresponding with areas of neovascularisation (indicated by T1-weighted contrast enhancement). Furthermore, these regions surround a core of highly increased $D_{1,2}$ and α, and decreased H_n that is likely related to necrosis, a feature of malignant glioma. The observation of high H_n in high-grade tumours is analogous to findings in DKI studies that report high mean κ to be representative of high tumour grade and malignancy (Falk Delgado et al., 2018). For the meningioma, its oedema is similar in $D_{1,2}$ to the low-grade glioma core and the high grade peripheral oedema, but the α is not so elevated as for infiltrative tumours. This may reflect the vasogenic rather than infiltrative oedema seen with meningiomas in comparison to intrinsic tumours. Additionally, the α and H_n of the meningioma are less distinctly different between the core and oedema. The differential patterns of these parameters may enable QDI to provide a rapid technique for aiding identification of tumour type and grade in the clinic.

4.5. Overcoming barriers to clinical translation of non-Gaussian diffusion MRI techniques

QDI overcomes the acquisition time limitation of non-Gaussian dMRI techniques to allow clinically feasible image acquisition. This innovation removes the clinical acquisition time barrier potentially enabling large-scale clinical studies and translation to clinical practice. We have shown that by addition of an ultra-high b-value shell to conventional dMRI protocols, QDWI and QDTI can be acquired in a clinically acceptable time using 3 and 6 diffusion direction protocols. We have also shown that the scan-rescan reproducibility of QDI model fits along diffusion gradient directions and QDWI and QDTI measures in regions of interest is high, albeit with greater accuracy and precision for acquisition protocols with greater numbers of diffusion gradient directions. Efficacy of 6 direction QDTI is shown by the lack of significant differences in tissue metrics and high reproducibility of metrics compared to 15 direction QDTI. Nevertheless there were significant differences in tissue values, and lower reproducibility of metrics, for QDWI when compared to QDTI data, potentially due to QDWI measures not being rotationally invariant. Despite this the mean $D_{1,2}$, and H_n maps consistently exhibited significantly greater tissue contrast than analogous DKI maps indicating that QDWI and QDTI data can be acquired quickly with sufficient image quality and measurement reproducibility for research and clinical applications.

Several recent reports describe fast DKI acquisition protocols for application in the clinic (Næss-Schmidt et al., 2018, 2017; Tietze et al., 2015; Yin et al., 2018). For example, Tietze et al. (2015) and Næss-Schmidt et al. (2018, 2017) used fast DKI (Hansen et al., 2013) to acquire data in 166s and 225s, respectively. This is in contrast to Yin et al. (2018) who used a conventional DKI protocol with multi-band imaging acceleration to acquire data in 130s. It should be noted that fast DKI (Hansen et al., 2013) only provides mean D_κ and mean κ and is therefore comparable to our 84s QDWI protocol. Furthermore, our 6 direction QDTI protocol was acquired quicker than each DKI study (i.e. 120s). If multi-band imaging was employed to accelerate dMRI acquisition our 15 direction QDTI could be acquired in approximately 120s, our 6 direction QDTI in approximately 60s, and QDWI in less than 60s, further supporting the potential clinical utility of the technique.

The QDI acquisition protocol described in this study uses high magnetic field gradients to acquire ultra-high b-value dMRI. Such high magnetic resonance field gradients are not ubiquitously available in the research or clinical setting and are a limitation of the current QDI protocol. Future studies are required to optimise QDI acquisition for lower maximum b-values to enable general application of the technique on research and clinical MR scanners.

5. Conclusion

We have presented theory and proof of concept for a novel quantitative dMRI technique that takes advantage of ultra-high b-values and minimal acquisition times. This QDI technique acquires images with analogous tissue contrast to DKI, whilst overcoming limitations of the DKI technique. QDI has been shown to generate potentially clinically meaningful tissue contrast, with both quantitative and anisotropy measures, in clinically acceptable acquisition times. Further studies are required to fully understand the capabilities of this new technique in tissue microstructural imaging but our initial findings suggest that QDI may be easily added to routine dMRI acquisitions allowing simple translation to the clinic.

Declaration of competing interest

The QDI technique is covered by UK patent application GB1909982.9 (inventors: Dr T.R. Barrick, Prof F.A. Howe, Dr M.G. Hall, Dr C. Ingo, Prof R.L. Magin). Patent pending August 28, 2019.

CRediT authorship contribution statement

Thomas R. Barrick: Conceptualization, Methodology, Software, Validation, Formal analysis, Investigation, Writing - original draft, Visualization, Supervision, Project administration, Funding acquisition. **Catherine A. Spilling:** Methodology, Software, Formal analysis, Investigation, Data curation, Writing - review & editing. **Carson Ingo:** Conceptualization, Methodology, Writing - review & editing. **Jeremy Madigan:** Resources, Writing - review & editing. **Jeremy D. Isaacs:** Resources, Writing - review & editing. **Philip Rich:** Resources, Writing - review & editing. **Timothy L. Jones:** Resources, Writing - review & editing. **Richard L. Magin:** Conceptualization, Writing - review & editing. **Matt G. Hall:** Conceptualization, Methodology, Writing - review & editing. **Franklyn A. Howe:** Conceptualization, Methodology, Investigation, Writing - review & editing, Supervision, Project administration, Funding acquisition.

Acknowledgments

Funding for this study was provided by a St George's, University of London Innovation Award. Additional funding for clinical data acquisition was provided by Innovate UK grant 103353 and a King's College London Alzheimer's Research UK Network Centre pump priming award. Thank you to Miss Lauren Binnie for SVD patient recruitment.

References

Albi, A., Pasternak, O., Minati, L., Marizzoni, M., Bartrés-Faz, D., Bargalló, N., Bosch, B., Rossini, P.M., Marra, C., Müller, B., Fiedler, U., Wiltfang, J., Roccatagliata, L., Picco, A., Nobili, F.M., Blin, O., Sein, J., Ranjeva, J.-P., Didic, M., Bombois, S., Lopes, R., Bordet, R., Gros-Dagnac, H., Payoux, P., Zoccatelli, G., Alessandrini, F., Beltramello, A., Ferretti, A., Caulo, M., Aiello, M., Cavaliere, C., Soricelli, A., Parnetti, L., Tarducci, R., Floridi, P., Tsolaki, M., Constantinidis, M., Drevelegas, A., Frisoni, G., Jovicich, J., The PharmaCog Consortium, 2017. Free water elimination improves test-retest reproducibility of diffusion tensor imaging indices in the brain: a longitudinal multisite study of healthy elderly subjects: free-Water Elimination improves DTI reproducibility. Hum. Brain Mapp. 38, 12–26. https://doi.org/10.1002/hbm.23350.

Alexander, D.C., 2008. A general framework for experiment design in diffusion MRI and its application in measuring direct tissue-microstructure features. Magn. Reson. Med. 60, 439–448. https://doi.org/10.1002/mrm.21646.

Alexander, D.C., Hubbard, P.L., Hall, M.G., Moore, E.A., Ptito, M., Parker, G.J.M., Dyrby, T.B., 2010. Orientationally invariant indices of axon diameter and density from diffusion MRI. Neuroimage 52, 1374–1389. https://doi.org/10.1016/j.neuroimage.2010.05.043.

Andersson, J.L.R., Graham, M.S., Zsoldos, E., Sotiropoulos, S.N., 2016. Incorporating outlier detection and replacement into a non-parametric framework for movement and distortion correction of diffusion MR images. Neuroimage 141, 556–572. https://doi.org/10.1016/j.neuroimage.2016.06.058.

Atkinson, H., Osselran, A., 2011. Rational solution for the time-fractional diffusion equation. SIAM J. Appl. Math. 71 (1), 92–106.

Ashburner, J., Friston, K.J., 2005. Unified segmentation. Neuroimage 26, 839–851. https://doi.org/10.1016/j.neuroimage.2005.02.018.

Assaf, Y., Basser, P.J., 2005. Composite hindered and restricted model of diffusion (CHARMED) MR imaging of the human brain. Neuroimage 27, 48–58. https://doi.org/10.1016/j.neuroimage.2005.03.042.

Assaf, Y., Blumenfeld-Katzir, T., Yovel, Y., Basser, P.J., 2008. Axcaliber: a method for measuring axon diameter distribution from diffusion MRI. Magn. Reson. Med. 59, 1347–1354. https://doi.org/10.1002/mrm.21577.

Bonet-Carne, E., Johnston, E., Daducci, A., Jacobs, J.G., Freeman, A., Atkinson, D., Hawkes, D.J., Punwani, S., Alexander, D.C., Panagiotaki, E., 2019. VERDICT-AMICO: ultrafast fitting algorithm for non-invasive prostate microstructure characterization. NMR Biomed. 32, e4019 https://doi.org/10.1002/nbm.4019.

Callaghan, P.T., 2011. Translational Dynamics and Magnetic Resonance: Principles of Pulsed Gradient Spin Echo NMR. Oxford University Press, Oxford.

Fractals and fractional calculus in continuum mechanics. In: first ed.Carpinteri, A., Mainardi, F. (Eds.), 1997, CISM International Centre for Mechanical Sciences. Springer-Verlag Wien.

Cheung, J.S., Wang, E., Lo, E.H., Sun, P.Z., 2012. Stratification of heterogeneous diffusion MRI ischemic lesion with kurtosis imaging: evaluation of mean diffusion and kurtosis MRI mismatch in an animal model of transient focal ischemia. Stroke 43, 2252–2254. https://doi.org/10.1161/STROKEAHA.112.661926.

Clark, C.A., Le Bihan, D., 2000. Water diffusion compartmentation and anisotropy at high b values in the human brain. Magn. Reson. Med. 44, 852–859. https://doi.org/10.1002/1522-2594(200012)44:6<852::AID-MRM5>3.0.CO;2-A.

Einstein, A., 1905. Über die von der molekularkinetischen Theorie der Wärme geforderte Bewegung von in ruhenden Flüssigkeiten suspendierten Teilchen. Ann. Phys. 322 (8), 549–560 (in German).

Evangelista, L.R., Lenzi, E.K., 2018. Fractional Diffusion Equations and Anomalous Diffusion. Cambridge University Press, Cambridge, UK, p. 345p.
Falk Delgado, Anna, Nilsson, M., van Westen, D., Falk Delgado, Alberto, 2018. Glioma grade discrimination with MR diffusion kurtosis imaging: a meta-analysis of diagnostic accuracy. Radiology 287, 119–127. https://doi.org/10.1148/radiol.2017171315.
Fischl, B., 2012. FreeSurfer. NeuroImage 62, 774–781. https://doi.org/10.1016/j.neuroimage.2012.01.021.
Gatto, R.G., Ye, A.Q., Colon-Perez, L., Mareci, T.H., Lysakowski, A., Price, S.D., Brady, S.T., Karaman, M., Morfini, G., Magin, R.L., 2019. Detection of axonal degeneration in a mouse model of Huntington's disease: comparison between diffusion tensor imaging and anomalous diffusion metrics. Magn. Reson. Mater. Phys. Biol. Med. 32 (4), 461–471. https://doi.org/10.1007/s10334-019-00742-6.
Gong, N.-J., Chan, C.-C., Leung, L.-M., Wong, C.-S., Dibb, R., Liu, C., 2017. Differential microstructural and morphological abnormalities in mild cognitive impairment and Alzheimer's disease: evidence from cortical and deep gray matter: macro- and microstructural changes in gray Matter of AD. Hum. Brain Mapp. 38, 2495–2508. https://doi.org/10.1002/hbm.23535.
Gorenflo, R., Mainardi, F., Moretti, D., Pagnini, G., Paradisi, P., 2002. Discrete random walk models for space–time fractional diffusion. Chem. Phys. 284, 521–541. https://doi.org/10.1016/S0301-0104(02)00714-0.
Gorenflo, R., Kilbas, A.A., Mainardi, F., Rogosin, S.V., 2014. Mittag-Leffler Functions, Related Topics and Applications. Springer-Verlag, Berlin, Germany, p. 443p, 2014.
Grebenkov, D.S., 2009. Laplacian eigenfunctions in NMR. II. Theoretical advances. Concepts Magn. Reson. 34A, 264–296. https://doi.org/10.1002/cmr.a.20145.
Grebenkov, D.S., 2008. Laplacian eigenfunctions in NMR. I. A numerical tool. Concepts Magn. Reson. 32A, 277–301. https://doi.org/10.1002/cmr.a.20117.
Greve, D.N., Fischl, B., 2009. Accurate and robust brain image alignment using boundary-based registration. Neuroimage 48, 63–72. https://doi.org/10.1016/j.neuroimage.2009.06.060.
Hall, M.G., Barrick, T.R., 2012. Two-step anomalous diffusion tensor imaging. NMR Biomed. 25, 286–294. https://doi.org/10.1002/nbm.1747.
Hansen, B., Lund, T.E., Sangill, R., Jespersen, S.N., 2013. Experimentally and computationally fast method for estimation of a mean kurtosis: fast Estimation of a Mean Kurtosis. Magn. Reson. Med. 69, 1754–1760. https://doi.org/10.1002/mrm.24743.
Haubold, H.J., Mathai, A.M., Saxena, R.K., 2011. Mittag-leffler functions and their applications. J. Appl. Math. 2011, 1–51. https://doi.org/10.1155/2011/298628.
Ingo, C., Barrick, T.R., Webb, A.G., Ronen, I., 2017. Accurate padé global approximations for the mittag-leffler function, its inverse, and its partial derivatives to efficiently compute convergent power series. Int. J. Appl. Comput. Math. 3, 347–362. https://doi.org/10.1007/s40819-016-0158-7.
Ingo, C., Magin, R., Parrish, T., 2014a. New insights into the fractional order diffusion equation using entropy and kurtosis. Entropy 16, 5838–5852. https://doi.org/10.3390/e16115838.
Ingo, C., Magin, R.L., Colon-Perez, L., Triplett, W., Mareci, T.H., 2014b. On random walks and entropy in diffusion-weighted magnetic resonance imaging studies of neural tissue: random Walks and Entropy in Diffusion-Weighted MRI. Magn. Reson. Med. 71, 617–627. https://doi.org/10.1002/mrm.24706.
Ingo, C., Sui, Y., Chen, Y., Parrish, T.B., Webb, A.G., Ronen, I., 2015. Parsimonious continuous time random walk models and kurtosis for diffusion in magnetic resonance of biological tissue. Front. Physiol. 3 https://doi.org/10.3389/fphy.2015.00011.
Jelescu, I.O., Budde, M.D., 2017. Design and validation of diffusion MRI models of white matter. Front. Physiol. 5 https://doi.org/10.3389/fphy.2017.00061.
Jelescu, I.O., Veraart, J., Adisetiyo, V., Milla, S.S., Novikov, D.S., Fieremans, E., 2015. One diffusion acquisition and different white matter models: how does microstructure change in human early development based on WMTI and NODDI? Neuroimage 107, 242–256. https://doi.org/10.1016/j.neuroimage.2014.12.009.
Jensen, J.H., 2018. Advanced DWI methods for the assessment of ischemic stroke. Am. J. Roentgenol. 210, 728–730. https://doi.org/10.2214/AJR.17.19223.
Jensen, J.H., Helpern, J.A., 2010. MRI quantification of non-Gaussian water diffusion by kurtosis analysis. NMR Biomed. 23, 698–710. https://doi.org/10.1002/nbm.1518.
Jensen, J.H., Helpern, J.A., Ramani, A., Lu, H., Kaczynski, K., 2005. Diffusional kurtosis imaging: the quantification of non-Gaussian water diffusion by means of magnetic resonance imaging. Magn. Reson. Med. 53, 1432–1440. https://doi.org/10.1002/mrm.20508.
Johansen-Berg, H., Behrens, T.E.J. (Eds.), 2009. Diffusion MRI, from Quantitative Measurement to in Vivo Neuroanatomy, second ed. Academic Press. 2014.
Jones, D.K., Knösche, T.R., Turner, R., 2013. White matter integrity, fiber count, and other fallacies: the do's and don'ts of diffusion MRI. Neuroimage 73, 239–254. https://doi.org/10.1016/j.neuroimage.2012.06.081.
Jurlewicz, A., Kern, P., Meerschaert, M.M., Scheffler, H.-P., 2012. Fractional governing equations for coupled random walks. Comput. Math. Appl. 64, 3021–3036. https://doi.org/10.1016/j.camwa.2011.10.010.
Karaman, M.M., Sui, Y., Wang, H., Magin, R.L., Li, Y., Zhou, X.J., 2016. Differentiating low- and high-grade pediatric brain tumors using a continuous-time random-walk diffusion model at high *b* -values: pediatric Brain Tumors Using a CTRW Diffusion Model. Magn. Reson. Med. 76, 1149–1157. https://doi.org/10.1002/mrm.26012.
Klages, R., Radons, G., Sokolov, I.M., 2008. Anomalous Transport: Foundations and Applications. Wiley, Weinheim.
Lemberskiy, G., Fieremans, E., Veraart, J., Deng, F.-M., Rosenkrantz, A.B., Novikov, D.S., 2018. Characterization of prostate microstructure using water diffusion and NMR relaxation. Front. Physiol. 6, 91. https://doi.org/10.3389/fphy.2018.00091.
Lu, D., Jiang, Y., Ji, Y., Zhou, I.Y., Mandeville, E., Lo, E.H., Wang, X., Sun, P.Z., 2018. Journal club: evaluation of diffusion kurtosis imaging of stroke lesion with hemodynamic and metabolic MRI in a rodent model of acute stroke. Am. J. Roentgenol. 210, 720–727. https://doi.org/10.2214/AJR.17.19134.
Luchko, Y., 2016. Entropy production rate of a one-dimensional alpha-fractional diffusion process. Axioms 5, 6. https://doi.org/10.3390/axioms5010006.
Luchko, Y., 2019. Subordination principles for the multi-dimensional space-time-fractional diffusion-wave equation. Theor. Probab. Math. Stat. 98, 127–147. https://doi.org/10.1090/tpms/1067.
Magin, R.L., Abdullah, O., Baleanu, D., Zhou, X.J., 2008. Anomalous diffusion expressed through fractional order differential operators in the Bloch–Torrey equation. J. Magn. Reson. 190, 255–270. https://doi.org/10.1016/j.jmr.2007.11.007.
Magin, R.L., Ingo, C., Colon-Perez, L., Triplett, W., Mareci, T.H., 2013. Characterization of anomalous diffusion in porous biological tissues using fractional order derivatives and entropy. Microporous Mesoporous Mater. 178, 39–43. https://doi.org/10.1016/j.micromeso.2013.02.054.
Magin, R.L., Karani, H., Wang, S., Liang, Y., 2019. Fractional order complexity model of the diffusion signal decay in MRI. Mathematics 7, 348. https://doi.org/10.3390/math7040348.
Mainardi, F., Luchko, Y., Pagnini, G., 2001. The fundamental solution of the space-time fractional diffusion equation. Fractional Calculus and Applied Analysis 4 (No 2), 153–192. http://www.math.bas.bg/fcaa. http://www.diogenes.bg/fcaa.
Mazo, R.M., 2009. Brownian Motion: Fluctuations, Dynamics, and Applications. Oxford University Press.
Meerschaert, M., Scheffler, H.P., 2019. Continuous time random walks and space-time fractional differential equations. In: Kochubei, A., Luchko, Y. (Eds.), Basic Theory. De Gruyter, Berlin, Boston, pp. 385–406. https://doi.org/10.1515/9783110571622-016.
Metzler, R., Klafter, J., 2000. The random walk's guide to anomalous diffusion: a fractional dynamics approach. Phys. Rep. 339, 1–77. https://doi.org/10.1016/S0370-1573(00)00070-3.
Metzler, R., Jeon, J.-H., Cherstvy, A.G., Barkai, E., 2014. Anomalous diffusion models and their properties: non-stationarity, non-ergodicity, and ageing at the centenary of single particle tracking. Phys. Chem. Chem. Phys. 16, 24128–24164. https://doi.org/10.1039/C4CP03465A.
Næss-Schmidt, E.T., Blicher, J.U., Eskildsen, S.F., Tietze, A., Hansen, B., Stubbs, P.W., Jespersen, S., Østergaard, L., Nielsen, J.F., 2017. Microstructural changes in the thalamus after mild traumatic brain injury: a longitudinal diffusion and mean kurtosis tensor MRI study. Brain Inj. 31, 230–236. https://doi.org/10.1080/02699052.2016.1229034.
Næss-Schmidt, E.T., Blicher, J.U., Tietze, A., Rask, C.U., Svendsen, S.W., Schröder, A., Thastum, M.M., Tuborgh, A.H., Frederiksen, O.-V., Østergaard, L., Eskildsen, S.F., Hansen, B., Jespersen, S., Nielsen, J.F., 2018. Diffusion MRI findings in patients with extensive and minimal post-concussion symptoms after mTBI and healthy controls: a cross sectional study. Brain Inj. 32, 91–98. https://doi.org/10.1080/02699052.2017.1377352.
Novikov, D.S., Fieremans, E., Jensen, J.H., Helpern, J.A., 2011. Random walk with barriers: diffusion restricted by permeable membranes. Nat. Phys. 7, 508–514. https://doi.org/10.1038/nphys1936.
Novikov, D.S., Jensen, J.H., Helpern, J.A., Fieremans, E., 2014. Revealing mesoscopic structural universality with diffusion. Proc. Natl. Acad. Sci. Unit. States Am. 111, 5088–5093. https://doi.org/10.1073/pnas.1316944111.
Novikov, D.S., Kiselev, V.G., 2010. Effective medium theory of a diffusion-weighted signal. NMR Biomed. 23, 682–697. https://doi.org/10.1002/nbm.1584.
Novikov, D.S., Kiselev, V.G., Jespersen, S.N., 2018a. On modeling. Magn. Reson. Med. 79, 3172–3193. https://doi.org/10.1002/mrm.27101.
Novikov, D.S., Veraart, J., Jelescu, I.O., Fieremans, E., 2018b. Rotationally-invariant mapping of scalar and orientational metrics of neuronal microstructure with diffusion MRI. Neuroimage 174, 518–538. https://doi.org/10.1016/j.neuroimage.2018.03.006.
Novikov, D.S., Fieremans, E., Jespersen, S.N., Kiselev, V.G., 2019. Quantifying brain microstructure with diffusion MRI: theory and parameter estimation. NMR Biomed. 32, e3998. https://doi.org/10.1002/nbm.3998.
Pajevic, S., Pierpaoli, C., 1999. Color schemes to represent the orientation of anisotropic tissues from diffusion tensor data: application to white matter fiber tract mapping in the human brain Magn. Reson. Med. 42, 526–540.
Panagiotaki, E., Chan, R.W., Dikaios, N., Ahmed, H.U., O'Callaghan, J., Freeman, A., Atkinson, D., Punwani, S., Hawkes, D.J., Alexander, D.C., 2015. Microstructural characterization of normal and malignant human prostate tissue with vascular, extracellular, and restricted diffusion for cytometry in tumours magnetic resonance imaging. Invest. Radiol. 50, 218–227. https://doi.org/10.1097/RLI.0000000000000115.
Panagiotaki, E., Walker-Samuel, S., Siow, B., Johnson, S.P., Rajkumar, V., Pedley, R.B., Lythgoe, M.F., Alexander, D.C., 2014. Noninvasive quantification of solid tumor microstructure using VERDICT MRI. Canc. Res. 74, 1902–1912. https://doi.org/10.1158/0008-5472.CAN-13-2511.
Pasternak, O., Sochen, N., Gur, Y., Intrator, N., Assaf, Y., 2009. Free water elimination and mapping from diffusion MRI. Magn. Reson. Med. 62, 717–730. https://doi.org/10.1002/mrm.22055.
Pierpaoli, C., Basser, P.J., 1996. Toward a quantitative assessment of diffusion anisotropy. Magn. Reson. Med. 36, 893–906. https://doi.org/10.1002/mrm.1910360612.
Praet, J., Manyakov, N.V., Muchene, L., Mai, Z., Terzopoulos, V., de Backer, S., Torremans, A., Guns, P.-J., Van De Casteele, T., Bottelbergs, A., Van Broeck, B., Sijbers, J., Smeets, D., Shkedy, Z., Bijnens, L., Pemberton, D.J., Schmidt, M.E., Van der Linden, A., Verhoye, M., 2018. Diffusion kurtosis imaging allows the early detection and longitudinal follow-up of amyloid-β-induced pathology. Alzheimer's Res. Ther. 10 https://doi.org/10.1186/s13195-017-0329-8.

Raja, R., Rosenberg, G., Caprihan, A., 2019. Review of diffusion MRI studies in chronic white matter diseases. Neurosci. Lett. 694, 198–207. https://doi.org/10.1016/j.neulet.2018.12.007.

Sigmund, E.E., Novikov, D.S., Sui, D., Ukpebor, O., Baete, S., Babb, J.S., Liu, K., Feiweier, T., Kwon, J., McGorty, K., Bencardino, J., Fieremans, E., 2014. Time-dependent diffusion in skeletal muscle with the random permeable barrier model (RPBM): application to normal controls and chronic exertional compartment syndrome patients: $D(t)$ with RPBM analysis in CECS patients. NMR Biomed. 27, 519–528. https://doi.org/10.1002/nbm.3087.

Tabesh, A., Jensen, J.H., Ardekani, B.A., Helpern, J.A., 2011. Estimation of tensors and tensor-derived measures in diffusional kurtosis imaging. Magn. Reson. Med. 65, 823–836. https://doi.org/10.1002/mrm.22655.

Tan, Y., Zhang, H., Wang, X., Qin, J., Wang, L., 2018. The value of multi ultra-high- b -value DWI in grading cerebral astrocytomas and its association with aquaporin-4. Br. J. Radiol. 91 https://doi.org/10.1259/bjr.20170696.

Tang, L., Zhou, X.J., 2019. Diffusion MRI of cancer: from low to high b-values: high b-Value Diffusion MRI of Cancer. J. Magn. Reson. Imag. 49, 23–40. https://doi.org/10.1002/jmri.26293.

Tax, C.M., Grussu, F., Kaden, E., Ning, L., Rudrapatna, U., Evans, J., St-Jean, S., Leemans, A., Koppers, S., Merhof, D., Ghosh, A., Tanno, R., Alexander, D.C., Zappalà, S., Charron, C., Kusmia, S., Linden, D.E., Jones, D.K., Veraart, J., 2019. Cross-scanner and cross-protocol diffusion MRI data harmonisation: a benchmark database and evaluation of algorithms. Neuroimage 195, 285–299. https://doi.org/10.1016/j.neuroimage.2019.01.077.

Tietze, A., Hansen, M.B., Østergaard, L., Jespersen, S.N., Sangill, R., Lund, T.E., Geneser, M., Hjelm, M., Hansen, B., 2015. Mean diffusional kurtosis in patients with glioma: initial results with a fast imaging method in a clinical setting. Am. J. Neuroradiol. 36, 1472–1478. https://doi.org/10.3174/ajnr.A4311.

Topgaard, D., 2017. Multidimensional diffusion MRI. J. Magn. Reson. 275, 98–113. https://doi.org/10.1016/j.jmr.2016.12.007.

Veraart, J., Fieremans, E., Novikov, D.S., 2019. On the scaling behavior of water diffusion in human brain white matter. Neuroimage 185, 379–387. https://doi.org/10.1016/j.neuroimage.2018.09.075.

von Kummer, R., Dzialowski, I., 2017. Imaging of cerebral ischemic edema and neuronal death. Neuroradiology 59, 545–553. https://doi.org/10.1007/s00234-017-1847-6.

Wheeler-Kingshott, C.A.M., Cercignani, M., 2009. About "axial" and "radial" diffusivities. Magn. Reson. Med. 61, 1255–1260. https://doi.org/10.1002/mrm.21965.

Xu, S., Ye, D., Lian, T., Cai, J., Xiao, Z., Huang, Y., Chen, X., Zhang, Z., 2016. Assessment of severity of leukoaraiosis: a diffusional kurtosis imaging study. Clin. Imag. 40, 732–738. https://doi.org/10.1016/j.clinimag.2016.02.018.

Xueying, L., Zhongping, Z., Zhoushe, Z., Li, G., Yongjin, T., Changzheng, S., Zhifeng, Z., Peihao, C., Hao, X., Li, H., 2015. Investigation of apparent diffusion coefficient from ultra-high b-values in Parkinson's disease. Eur. Radiol. 25, 2593–2600. https://doi.org/10.1007/s00330-015-3678-3.

Yin, J., Sun, H., Wang, Z., Ni, H., Shen, W., Sun, P.Z., 2018. Diffusion kurtosis imaging of acute infarction: comparison with routine diffusion and follow-up MR imaging. Radiology 287, 651–657. https://doi.org/10.1148/radiol.2017170553.

Yingnan, X., Zhenhua, Z., Caiyun, W., Huiru, L., Suyuan, W., Jiance, L., Qichuan, Z., Weijian, C., Qiong, Y., 2018. Characterization of Alzheimer's disease using ultra-high b-values apparent diffusion coefficient and diffusion kurtosis imaging. Aging Dis 10 (5), 1026–1036. https://doi.org/10.14336/AD.2018.1129.

Zaslavsky, G.M., 2005. Hamiltonian Chaos and Fractional Dynamics. Oxford University Press, New York.

Zhang, H., Schneider, T., Wheeler-Kingshott, C.A., Alexander, D.C., 2012. NODDI: practical in vivo neurite orientation dispersion and density imaging of the human brain. Neuroimage 61, 1000–1016. https://doi.org/10.1016/j.neuroimage.2012.03.072.

Zhu, L.-H., Zhang, Z.-P., Wang, F.-N., Cheng, Q.-H., Guo, G., 2019. Diffusion kurtosis imaging of microstructural changes in brain tissue affected by acute ischemic stroke in different locations. Neural Regen. Res. 14, 272. https://doi.org/10.4103/1673-5374.244791.